AIAA JOURNAL
Vol. 52, No. 9, September 2014

Application of Gaussian Moment Closure to Microscale Flows with Moving Embedded Boundaries

J. G. McDonald,* J. S. Sachdev,† and C. P. T. Groth‡
University of Toronto, Toronto, Ontario M3H 5T6, Canada

DOI: 10.2514/1.J052576

The application of the Gaussian moment closure to continuum and microscale flows with embedded, and possibly moving, boundaries is considered. The Gaussian moment closure is briefly reviewed, as is an extension that allows for the treatment of flow of diatomic gases. A parallel upwind, finite volume scheme with adaptive mesh refinement using a Roe-type numerical flux function is described for solving the hyperbolic system of partial differential equations arising from this closure on multiblock meshes with embedded and possibly moving boundaries. The purely hyperbolic nature of moment equations makes them particularly insensitive to discretizations involving grids with irregularities. Typical of adaptive mesh-refinement, embedded-boundary, and Cartesian cut-cell treatments, mesh irregularities are difficult to deal with when second derivatives are required by the physical model. Such is the case for the Navier–Stokes equations. Numerical solutions to mathematical descriptions involving second derivatives show significantly degraded solution quality as compared to solutions of first-order quasi-linear moment equations. Solid-wall boundary conditions are implemented via a Knudsen-layer approximation. Comparisons are made between numerical solutions of the Gaussian model on both body-fitted meshes and meshes with embedded boundaries, as well as to experimental and approximate analytic results for a variety of flow problems. The benefits and potential of the proposed approach for unsteady microscale flow applications having complex geometries are clearly demonstrated.

Nomenclature

A	=	computational cell area
a_i	=	External acceleration field
$\boldsymbol{c}_i$	=	particle random velocity vector; $v_i - u_i$
d	=	plate gap width and cylinder diameter
E_r	=	molecular rotational-energy density
$\boldsymbol{F}$	=	vector of x-direction fluxes
$\mathcal{F}$	=	probability density function
f	=	frequency
$\boldsymbol{G}$	=	vector of y-direction fluxes
$\mathcal{G}$	=	Gaussian distribution function
$\mathcal{G}_D$	=	Gaussian distribution function for diatomic gas
$\boldsymbol{H}$	=	flux dyad; $[\boldsymbol{F}, \boldsymbol{G}]$
I	=	molecular moment of inertia
k	=	Boltzmann's constant
Kn	=	flow Knudsen number
ℓ	=	reference length scale
$\mathcal{M}$	=	Maxwell–Boltzmann distribution function
M	=	Velocity-dependent weight
Ma	=	flow Mach number
m	=	gas-particle mass
$\boldsymbol{n}$	=	unit normal
p	=	thermodynamic pressure
Re	=	flow Reynolds number
$\boldsymbol{S}$	=	source vector
S	=	speed ratio
T	=	temperature
t	=	time
$\boldsymbol{U}$	=	vector of moments
u_i	=	bulk velocity
$\boldsymbol{v}_i$	=	gas-particle velocity vector
$\boldsymbol{w}$	=	velocity of a cell face
$\boldsymbol{x}_i$	=	position vector
α	=	accommodation coefficient
$\boldsymbol{\Gamma}_\alpha$	=	vector of velocity-dependent weights
γ	=	ratio of heat capacities
$\Delta\ell$	=	length of a cell face
Θ_{ij}	=	anisotropic temperature tensor
$\boldsymbol{\Lambda}_\alpha$	=	vector of closure coefficients
λ	=	mean free path
μ, μ_B	=	dynamic and bulk viscosity
ρ	=	gas density
τ, τ_t, τ_r	=	general, translational, and rotational relaxation times
ω_α	=	molecular angular velocity

Received 22 January 2013; revision received 20 January 2014; accepted for publication 11 March 2014; published online 21 July 2014.

*Institute for Aerospace Studies, 4925 Dufferin Street; currently Department of Mechanical Engineering, University of Ottawa, Ottawa, Ontario K1N 6N5, Canada; james.mcdonald@uottawa.ca.

†Institute for Aerospace Studies, 4925 Dufferin Street; currently Combustion Research and Flow Technology, Pipersville, PA 18947; j.sachdev@utoronto.ca. Member AIAA.

‡Professor, Institute for Aerospace Studies, 4925 Dufferin Street; groth@utias.utoronto.ca. Senior Member AIAA.

I. Introduction

NONEQUILIBRIUM microscale flows, such as those encountered in the complex microsized conduits of microelectromechanical systems and flows associated with chemical-vapor deposition, are difficult to solve using existing mathematical models and numerical methods [1,2]. In most cases, these microscale flows are in the subsonic to low-supersonic regimes and, due to their microgeometries, have low Reynolds numbers Re and remain laminar. Flow Knudsen numbers Kn in the range $0.01 < Kn < 10$ may be encountered, even for pressures above one atmosphere, and as a result, noncontinuum and thermal nonequilibrium effects can significantly influence momentum and heat transfer phenomena in typical microchannel flows [3,4]. The situation is further complicated by the fact that, in many practical cases, microscale flows can involve complex moving and/or evolving boundaries and this can require special gridding techniques.

Particle-simulation techniques, such as the direct-simulation Monte Carlo method [2,5,6], and techniques based on the direct discretization of the kinetic equation, such as the approach proposed by Mieussens [7], have been developed for the prediction of general nonequilibrium gaseous flows. However, for near-continuum through to transitional-regime flows and for flows with low Mach numbers, the computational costs incurred by these techniques are considerable and have prohibited their widespread usage [2,6]. Alternate approaches that show considerable promise for the

treatment of microscale flows are based on moment closures of the Boltzmann equation [8–12]. Moment closures provide an extended set of hyperbolic partial differential equations (PDEs) describing the transport of macroscopic fluid properties. In general, the solution of these PDEs requires considerably less computational effort than obtaining solutions using a particle-simulation or direct-discretization methods.

The treatment of nonequilibrium flows with a purely hyperbolic model brings additional advantages from a computational perspective. The hyperbolic moment equations involve only first-order derivatives (this is in contrast to other transport equations that have an elliptic nature and require the evaluation of second- and/or higher-order derivatives) and are therefore well suited to solution by the class of very successful Godunov-type finite volume schemes that make use of adaptive mesh refinement (AMR) with treatments for embedded and moving boundaries and interfaces [12–24]. For hyperbolic systems, schemes of this type are robust, relatively insensitive to irregularities in the computational grids, provide accurate resolution of discontinuities, and permit the systematic application of physically realistic boundary conditions. When coupled with AMR, embedded boundaries permit treatment of complex and evolving flow geometries and the resolution of highly disparate length scales while at the same time optimizing the usage of computational resources. These numerical schemes also have narrow stencils, making them suitable for implementation on massively parallel computer architectures [19–21,23–28]. Note that higher than first-order derivatives can be problematic when using adaptive mesh refinement or meshes with embedded boundaries, as irregularities in the grid can make accurate evaluation of these derivatives difficult. In particular, there are serious tradeoffs between accuracy and positivity (related to the satisfaction of the maximum principal) of the spatial discretization operator for discretizations of second-order derivatives [29,30]. Both accurate and positive discretizations of the Laplacian operator can be difficult to achieve on computational meshes having large variations in the sizes of adjacent cells, as can typically occur in AMR techniques. This situation is avoided with hyperbolic moment closures.

With this viewpoint in mind, the potential of hyperbolic moment closures combined with Godunov finite volume discretizations, AMR, and embedded boundaries is explored herein for the efficient and accurate simulation of continuum and nonequilibrium microscale flows with moving boundaries and interfaces. Numerical solutions of the Gaussian closure [9,21,31,32] (a low-order member of the Levermore hierarchy) are considered. Following a brief review of the Gaussian closure, a novel parallel finite volume scheme with AMR and Riemann-solver-based numerical flux function is described and used for solving the Gaussian moment equations on multiblock meshes with embedded and possibly moving boundaries [23,24]. After establishing the accuracy of the finite volume scheme and AMR scheme with embedded-boundary treatment, numerical predictions are then examined for a number of flow problems with embedded and/or evolving boundaries in both the continuum and transitional regimes. The results well illustrate the potential of moment closures and demonstrate the benefits of a purely hyperbolic treatment.

II. Governing Transport Equations

A. Method of Moments

A probabilistic treatment is adopted in classical gas-kinetic theory in order to represent the microscopic behavior of gases and model noncontinuum flows. This is accomplished by defining a probability density function for the gas, $\mathcal{F}(x_i, v_i, t)$, in six-dimensional phase space that reflects the probability of finding particles at a given location x_i and time t having a velocity v_i. The time evolution of $\mathcal{F}$ is governed by the Boltzmann equation [33–35], an integrodifferential equation having the form

$$\frac{\partial \mathcal{F}}{\partial t} + v_i \frac{\partial \mathcal{F}}{\partial x_i} + a_i \frac{\partial \mathcal{F}}{\partial v_i} = \frac{\delta \mathcal{F}}{\delta t} \tag{1}$$

where a_i is the acceleration due to external forces and is taken to be zero in the present work. The term on the right-hand side of the equation, $\delta\mathcal{F}/\delta t$, is the Boltzmann collision operator representing the time rate of change of the distribution function produced by binary interparticle collisions. This term involves a multidimensional integral over both velocity space and solid angle and can, in many cases, be challenging to evaluate. Fortunately, for many engineering applications, the detailed evaluation of the collision operator can be avoided by using simplifying approximations such as the relaxation time or Bhatnagar–Gross–Krook (BGK) model, as first proposed by Bhatnagar et al. [36]. In the relaxation-time model, the collision operator is represented by a source term

$$\frac{\delta \mathcal{F}}{\delta t} = -\frac{\mathcal{F} - \mathcal{M}}{\tau} \tag{2}$$

where $\mathcal{M}$ is the well-known Maxwell–Boltzmann distribution, the equilibrium solution to the Boltzmann equation toward which the nonequilibrium solution is relaxing; and τ is a characteristic relaxation time for the collision processes. The relaxation time can be related to the Knudsen number Kn, and a reference length scale ℓ using $Kn = \lambda/\ell$ and $v_{\text{th}} = \lambda/\tau$, where v_{th} is the mean or thermal speed of the particles and λ is the mean free path traveled by the particles between collisions. Thus,

$$\tau = \frac{\lambda}{v_{\text{th}}} = \frac{Kn\ell}{v_{\text{th}}} \tag{3}$$

showing that the relaxation time scales directly with Knudsen number.

The BGK operator of Eq. (2) is only an approximation to the Boltzmann collision integral and ignores the detailed nature of interparticle interactions. Nevertheless, it retains many of the qualitative features of the true collision integral and is thought to be sufficient for the present study of microscale flows. In particular, the relaxation-time approximation preserves the usual collisional invariants and, under equilibrium conditions ($Kn \to 0$ and $\tau \to 0$), dictates that $\delta\mathcal{F}/\delta t = 0$ and $\mathcal{F} = \mathcal{M}$ as required. For collisionless flows ($Kn \to \infty$ and $\tau \to \infty$), the timescales of interest are much smaller than τ and $\delta\mathcal{F}/\delta t \approx 0$, also as expected.

Macroscopic or "observable" properties of the gas can be obtained by taking appropriate velocity moments of $\mathcal{F}$. This is done by multiplying the distribution function by a velocity-dependent weight M and integrating over all velocity space. For example, if the gas-particle mass m is chosen as the weight, the corresponding velocity moment is the fluid density given by

$$\rho = \int_{-\infty}^{\infty} m\mathcal{F}(x_i, v_i, t)\, \mathrm{d}^3 v = \langle m\mathcal{F} \rangle \tag{4}$$

Other moments of interest include the bulk velocity

$$u_i = \frac{< m v_i \mathcal{F} >}{\rho} \tag{5}$$

and anisotropic pressure tensor

$$P_{ij} = < m c_i c_j \mathcal{F} > \tag{6}$$

Here, $c_i = v_i - u_i$ is the random component of particle velocity. The deviatoric stress tensor τ_{ij} is related to the pressure tensor as $\tau_{ij} = \delta_{ij} p - P_{ij}$, where $p = P_{ii}/3$ is the thermodynamic pressure.

Transport equations governing the time evolution of the macroscopic quantities can be derived by evaluating velocity moments of the Boltzmann equation given in Eq. (1). This yields the so-called Maxwell's equation of change [35] describing the transport of the moment $\langle M\mathcal{F} \rangle$, which can be expressed in weak conservation form as

$$\frac{\partial}{\partial t}\langle M\mathcal{F} \rangle + \frac{\partial}{\partial x_i}\langle v_i M\mathcal{F} \rangle = -\frac{1}{\tau}[\langle M\mathcal{F} \rangle - \langle M\mathcal{M} \rangle] \tag{7}$$

where the BGK collision operator has been used in the evaluation of the collision terms.

Investigation of Eq. (7) reveals that the method of moments for the macroscopic quantities does not yield a closed set of PDEs. This is due to the fact that the time evolution of one moment $\langle M\mathcal{F}\rangle$ depends on the divergence of a moment of one order higher in velocity $\langle v_i M\mathcal{F}\rangle$. However, the time evolution of this higher-order moment depends on the spatial derivatives of a velocity moment of even higher order. This process continues ad infinitum, and the application of the method of moments to a general nonequilibrium gas would therefore seem to require the solution of an infinite number of coupled PDEs. This is obviously not practical.

B. Grad-Type Moment Closures

The most common technique for obtaining a closed system of moment equations for practical applications is to use an assumed form for the distribution function. That is to say, $\mathcal{F}$ is only allowed to deviate from equilibrium in a prescribed fashion. Higher-order moments then automatically become functions of lower-order moments, and the system of equations is closed.

Perhaps the most well-known assumed form for the nonequilibrium distribution function is that due to Grad [8,11]. Grad-type perturbative expansions for $\mathcal{F}$ are constructed about the equilibrium solution $\mathcal{M}$ through the use of Hermite polynomials that can be expressed more generally as a regular polynomial expansion of the form

$$\mathcal{F} = \mathcal{M}[1 + A + B_\alpha c_\alpha + C_{\alpha\beta} c_\alpha c_\beta + D_{\alpha\beta\gamma} c_\alpha c_\beta c_\gamma + \cdots] \tag{8}$$

where A, B_α, $C_{\alpha\beta}$, and $D_{\alpha\beta\gamma}$ are expansion coefficients. These coefficients depend on macroscopic fluid properties but are independent of the particle random velocities. Depending on the accuracy of the approximation that is required, the expansion is truncated to some prescribed order or degree in velocity space. This results in a closed system of PDEs governing the evolution of a finite set of macroscopic fluid quantities.

Although Grad-type expansions result in a closed set of hyperbolic transport equations for a finite set of velocity moments, the assumed distribution function can in many cases be nonphysical. It is possible for Eq. (8) to yield negative probabilities for some values of the particle velocity. This is particularly true in the tails of the distribution function for large random velocities. More significantly, closure breakdown and nonhyperbolicity of the moment equations can occur even for physically realizable moments close to local equilibrium. As a consequence, the moment equations can become ill-posed for initial-value problems, a property that is obviously highly undesirable [37,38]. The development of significant nonpositive portions of the distribution function and the loss of hyperbolicity of the moment equations tend to occur at roughly the same time, and these two issues may be related. Cai et al. [39] have very recently considered alterations of Grad-type closures in order to yield globally hyperbolic transport equations for arbitrary order expansions; however, the viability and accuracy of such an approach for a modest number of moments is questionable.

C. Gaussian Closure for a Monatomic Gas

Levermore [9] has proposed an alternative hierarchy of nonperturbative maximum-entropy moment closures with many desirable mathematical properties, including a positive-valued distribution function, hyperbolic moment equations, realizability of predicted moments, and a definable entropy relation [9,10,12]. This closure hierarchy is also based on an assumed form for the distribution function; however, in this case, $\mathcal{F}$ is assumed to have the form of a maximum-entropy distribution given by

$$\mathcal{F} = e^{\Lambda_\alpha \Gamma_\alpha} \tag{9}$$

where the closure coefficients Λ_α are functions of the prescribed macroscopic moments of interest, and Γ_α are velocity-dependent polynomial basis functions that are chosen following a procedure proposed by Levermore [9]. The maximum-entropy distribution is defined to be the distribution that maximizes the physical entropy subject to the constraint that it be consistent with a given finite set of velocity moments [9,10,12]. It may also be viewed as the most likely distribution function subject to the constraint that it yield a given finite set of moments [22,40]. Maximum-entropy formalisms have also been applied in a wide range other fields, from the modeling of liquid spray formation [41] to the prediction of radiative heat transfer [42–46]. Although maximum-entropy closures could be equally referred to as "minimum-entropy" closures, as they formally correspond to the distribution function having the minimum mathematical entropy for a given set of moments, the more commonly used term "maximum-entropy" is applied herein in reference to the closures' maximization of physical entropy.

For a monatomic gas, the Levermore hierarchy included 5-, 10-, 14-, 21-, 26-, and 35-moment closures [9]. The lowest order of these closures, other than the five-moment local-equilibrium closure resulting in the Euler equations of compressible gas dynamics, is the 10-moment or Gaussian closure. It is constructed by using the basis functions

$$\Gamma_\alpha = \{1, c_i, c_i c_j\} \tag{10}$$

This leads to a closed-form analytical expression for the assumed form of the distribution function, the Gaussian distribution $\mathcal{G}$, given by

$$\mathcal{F} = \mathcal{G} = \frac{\rho}{m(2\pi)^{3/2}(\det\Theta)^{1/2}} \exp\left(-\frac{1}{2}\Theta_{ij}^{-1} c_i c_j\right) \tag{11}$$

where $\Theta_{ij} = P_{ij}/\rho$ is defined to be the anisotropic "temperature" tensor. The Gaussian distribution appears to have been first derived in early work by Maxwell [47] and then rediscovered in subsequent but independent research by both Schlüter [48,49] and Holway [50–53]. It may be regarded as a generalization of the bi- and tri-Maxwellian velocity distribution functions with a form that does not require the identification of the planes of principal stress. This approximate nonequilibrium distribution possesses a Gaussian-like distribution in each of the principal strain axes. Physically, it corresponds to a nonequilibrium condition with a different temperature in each direction.

The Gaussian closure yields a strictly hyperbolic set of macroscopic transport equations that, in addition to equations for the gas density ρ and momentum ρu_i, contain equations for the symmetric nonequilibrium pressure tensor P_{ij}. Note that, by construction, the third-order velocity moments of the Gaussian are zero, $< mc_i c_j c_k \mathcal{G} > = 0$, such that the heat flux vector, $q_i = \frac{1}{2} < mc_i c_j c_j \mathcal{G} >$, also vanishes. This points to a somewhat significant limitation of the Gaussian closure: its inability to account for the effects of heat transfer. Nevertheless, this low-order closure is very representative of what may be achieved with hyperbolic closures of the type proposed by Levermore [9] and is therefore considered here. In particular, preliminary numerical studies by Brown et al. [31,32], McDonald and Groth [12,21,22,54], Lam and Groth [55], Suzuki and van Leer [56], Suzuki et al. [57], and Barth [58] indicate that closures of this type hold considerable promise for describing nonequilibrium transport, at least for subsonic and transonic flows in the slip and transition regimes.

Before continuing, it should be mentioned that, although the maximum-entropy closures of the Levermore [9] hierarchy possess many desirable properties, several difficulties are encountered in the practical application of the closures beyond the level of the Gaussian model. First, a numerical approach is required to relate the coefficients of the maximum entropy distribution Λ_α to the predicted macroscopic moments, as explicit analytical expressions are not achievable [9]. This significantly increases the computational costs of carrying out a computation using the closures. Even more problematic, Junk [59], Junk and Unterreiter [60], Schneider [61], and Hauck et al. [62] have shown that there are physically admissible regions of solution space defined by the velocity moments for which the entropy minimization problem is not solvable and the closure coefficients cannot be obtained. This is not a desirable feature for practical

computations of nonequilibrium flows, and it has prevented the wider application of the closures. Possible solutions or remedies for dealing with the nonrealizability of maximum-entropy closures have been proposed recently by Au [63], Schneider [61], Hauck et al. [62], and McDonald and Groth [12,22,64], and they appear to hold considerable promise. Groth et al. [65,66] have also proposed an alternative hierarchy of perturbative closures based on the Gaussian closure with a view to achieving practical and reliable mathematical tools for computation. Nevertheless, the focus of this study is to highlight what may be achieved with a hyperbolic description of nonequilibrium flows combined with an effective AMR finite volume numerical solution strategy, and the development of appropriate high-order closures will be the subject of future research.

D. Gaussian Closure for a Diatomic Gas

The preceding description is valid for a monatomic gas having no internal degrees of freedom or energy modes. An extension to the standard Gaussian closure for monatomic gases as proposed by Hittinger [67] allows for the treatment of diatomic gases and is used in this work. A similar extension that allows for polyatomic gases has also been proposed by Le Tallec [68]. The diatomic Gaussian closure comes from assuming the following form for the velocity probability density function:

$$\mathcal{G}_D = \frac{\rho I}{m^2(2\pi)^{5/2}(\det\Theta)^{1/2}(p/\rho)}\left(\frac{T}{T_r}\right) \times \exp\left[-\frac{1}{2}(\Theta_{ij}^{-1}c_i c_j + R_{\alpha\beta}\omega_\alpha\omega_\beta)\right] \tag{12}$$

where ω_α is the angular velocity vector of the molecule with just two nonvanishing components, I is the moment of inertia of a gas molecule, p is again the usual thermodynamic pressure, T is now the temperature associated with the translational energy, T_r is the rotational temperature, and $R_{\alpha\beta} = (\rho I/mp)(T/T_r)\delta_{\alpha\beta}$. Following McDonald and Groth [21,22] and Hittinger [67], a modified relaxation-time approximation for the collision operator can be used to represent interparticle collisions given by

$$\frac{\delta\mathcal{F}}{\delta t} = -\frac{\mathcal{F}-\mathcal{E}_D}{\tau_t} - \frac{\mathcal{E}_D - \mathcal{M}_D}{\tau_r} \tag{13}$$

where it is assumed that the nonequilibrium distribution relaxes toward a distribution $\mathcal{E}_D$ having translational degrees of freedom that are in equilibrium with each other but not in equilibrium with the rotational degrees of freedom. The equilibrium Maxwellian distribution in this case for a diatomic gas $\mathcal{M}_D$ has the form

$$\mathcal{M}_D = \frac{\rho I}{m^2(2\pi)^{5/2}(p/\rho)^{5/2}}\exp\left[-\frac{1}{2}\frac{\rho}{p}\left(c^2 + \frac{I}{m}\omega^2\right)\right] \tag{14}$$

The preceding model allows different relaxation times for the translational and rotational modes, τ_t and τ_r, and simple approximate expressions can be used to relate the relaxation times to the gas viscosities:

$$\tau_t = \frac{\mu}{p}, \qquad \tau_r = \frac{15\mu_B}{4p} \tag{15}$$

where μ is the fluid viscosity, and μ_B is the bulk viscosity; empirical relations can be used to determine the related viscosities. Generally, τ_r is larger but of the same order of magnitude as τ_t.

It is worth mentioning that further extensions of the Gaussian closure are possible to correct the defect in the missing heat flux. A regularization technique has been developed recently by McDonald and Groth [54] similar to that proposed by Struchtrup and Torrilhon [11,69] and can be applied to incorporate anisotropic thermal-diffusion effects. However, the regularization approach disrupts the quasi-linear hyperbolic form of the model and leads to an extended nonhyperbolic fluid-dynamic description with high-order derivatives having an elliptic nature. This is considered to be deleterious in the context of the AMR and moving boundary treatment considered herein due to the challenges in accurately evaluating higher than first-order derivatives on irregular meshes. A strictly hyperbolic treatment is deemed to be most desirable and, for this reason, the regularized extension of the Gaussian closure is not considered here.

E. Gaussian Closure Moment Equations

The moment equations arising from the Gaussian closure for a diatomic gas can be written as

$$\frac{\partial}{\partial t}(\rho) + \frac{\partial}{\partial x_i}(\rho u_i) = 0 \tag{16}$$

$$\frac{\partial}{\partial t}(\rho u_i) + \frac{\partial}{\partial x_j}(\rho u_i u_j + P_{ij}) = 0 \tag{17}$$

$$\frac{\partial}{\partial t}(\rho u_i u_j + P_{ij}) + \frac{\partial}{\partial x_k}(\rho u_i u_j u_k + u_i P_{jk} + u_j P_{ik} + u_k P_{ij}) = -\frac{1}{\tau_t}\left(P_{ij} - \frac{\delta_{ij}}{3}P_{kk}\right) - \frac{2}{15\tau_r}(P_{kk} - 3E_r)\delta_{ij} \tag{18}$$

$$\frac{\partial}{\partial t}(E_r) + \frac{\partial}{\partial x_i}(u_i E_r) = -\frac{1}{5\tau_r}(3E_r - P_{kk}) \tag{19}$$

where E_r is the rotational energy given by $E_r = p(T_r/T)$. A very similar but reduced set of transport equations can be obtained for monatomic gases. For nonequilibrium flows in two space dimensions, the Gaussian moment equations can be reexpressed in weak conservation form as

$$\frac{\partial \boldsymbol{U}}{\partial t} + \frac{\partial \boldsymbol{F}}{\partial x} + \frac{\partial \boldsymbol{G}}{\partial y} = \boldsymbol{S} \tag{20}$$

where x and y are the coordinates of the two-dimensional Cartesian frame, and $\boldsymbol{U}$ is the vector of conserved solution variables given by

$$\boldsymbol{U} = [\rho,\ \rho u_x,\ \rho u_y,\ \rho u_x^2 + P_{xx},\ \rho u_x u_y + P_{xy},\ \rho u_y^2 + P_{yy},\ P_{zz},\ E_r]^T$$

Here, $\boldsymbol{F}$ and $\boldsymbol{G}$ are x- and y-direction components of the solution flux dyad $\boldsymbol{H} = [\boldsymbol{F}, \boldsymbol{G}]$ having the forms

$$\boldsymbol{F} = \begin{bmatrix} \rho u_x \\ \rho u_x^2 + P_{xx} \\ \rho u_x u_y + P_{xy} \\ \rho u_x^3 + 3u_x P_{xx} \\ \rho u_x^2 u_y + 2u_x P_{xy} + u_y P_{xx} \\ \rho u_x u_y^2 + u_x P_{yy} + 2u_y P_{xy} \\ u_x P_{zz} \\ u_x E_r \end{bmatrix}, \quad \boldsymbol{G} = \begin{bmatrix} \rho u_y \\ \rho u_x u_y + P_{xy} \\ \rho u_y^2 + P_{yy} \\ \rho u_x^2 u_y + 2u_x P_{xy} + u_y P_{xx} \\ \rho u_x u_y^2 + u_x P_{yy} + 2u_y P_{xy} \\ \rho u_y^3 + 3u_y P_{yy} \\ u_y P_{zz} \\ u_y E_r \end{bmatrix}$$

and $\boldsymbol{S}$ is the source vector associated with collisional processes given by

$$\boldsymbol{S} = \begin{bmatrix} 0 \\ 0 \\ 0 \\ -\frac{1}{3\tau_t}(2P_{xx} - P_{yy} - P_{zz}) - \frac{2}{15\tau_r}(P_{xx} + P_{yy} + P_{zz} - 3E_r) \\ -\frac{1}{\tau_t}P_{xy} \\ -\frac{1}{3\tau_t}(2P_{yy} - P_{xx} - P_{zz}) - \frac{2}{15\tau_r}(P_{xx} + P_{yy} + P_{zz} - 3E_r) \\ -\frac{1}{3\tau_t}(2P_{zz} - P_{xx} - P_{yy}) - \frac{2}{15\tau_r}(P_{xx} + P_{yy} + P_{zz} - 3E_r) \\ -\frac{1}{5\tau_r}(3E_r - P_{xx} - P_{yy} - P_{zz}) \end{bmatrix}$$

In the preceding equations, u_x and u_y are the velocity components in the x and y directions; and P_{xx}, P_{xy}, P_{yy}, and P_{zz} are the four nonzero components of the pressure tensor in the restrictive case of two-dimensional flows.

F. Solid-Wall Boundary Conditions

The prescription of boundary data for the Gaussian model requires some consideration due to the increased number of dependent solution variables. For the microscale flows of interest, a Knudsen-layer analysis is used to arrive at boundary conditions for solid walls, which allows for velocity slip [8,21]. In this approach, it is assumed that there exists a Knudsen layer next to the solid surface. In this infinitesimally thin layer, the fluid exists as a combination of the distribution function defining incoming particles from the interior flowfield and a distribution function defining reflected particles arising from the wall. For example, for a solid wall extending in the x direction with a fluid above it, all the particles with negative y-direction velocities in the Knudsen layer will come from the neighboring fluid with statistical properties defined by the Gaussian. To model the particle interaction with the wall, an accommodation coefficient, $0 \le \alpha \le 1$, is then defined. If α is zero (specular reflection), the incoming particles will simply be reflected specularly from the wall back into the Knudsen layer. For $\alpha = 1$ (diffuse reflection), incoming particles are fully accommodated and will therefore come into thermodynamic equilibrium with the wall before being released from the wall and will reenter the Knudsen layer with the statistical properties of a Maxwell–Boltzmann distribution defined by a wall temperature T_w. For any intermediate α value, the reflected particles will enter the Knudsen layer as a combination of the two cases. The resulting distribution function in the Knudsen layer is then given by

$$\mathcal{F}_{Kn} = \mathcal{F}_+ + \mathcal{F}_- \tag{21}$$

where $\mathcal{F}_+$ and $\mathcal{F}_-$ are given by

$$\mathcal{F}_- = \begin{cases} \mathcal{G}_b(v_x, v_y, v_z) & \text{for } v_y < 0, \\ 0 & \text{for } v_y > 0, \end{cases}$$

$$\mathcal{F}_+ = \begin{cases} \alpha\mathcal{M}_w(v_x, v_y, v_z) + (1-\alpha)\mathcal{G}_b(v_x, -v_y, v_z) & \text{for } v_y > 0, \\ 0 & \text{for } v_y < 0, \end{cases}$$

where $\mathcal{G}_b$ is the Gaussian distribution at the edge of the Knudsen layer, and where $\mathcal{M}_w$ is the Maxwellian defining particles that are fully accommodated by the wall. By assuming that the bulk y-direction velocity of the fluid immediately above the wall is zero and by imposing the constraint that the net particle flux through the wall is also necessarily zero, it is possible to show that the Maxwellian defining accommodated particles has the form

$$\mathcal{M}_w(v_x, v_y, v_z) = \frac{\rho\sqrt{mP_{yy}/\rho kT_w}}{m(2\pi)^{3/2}(m/kT_w)^{3/2}} \times \exp\left\{-\left(\frac{m}{2kT_w}\right)[(v_x - u_{x_w})^2 + v_y^2 + v_z^2]\right\} \tag{22}$$

where k is Boltzmann's constant, and all macroscopic quantities appearing in the preceding expression are those of the fluid outside the Knudsen layer with the exception of the wall temperature T_w and the velocity component of the wall in the x direction u_{x_w}. A quick inspection of the first term in this distribution function finds that it relates the density of the reflected Maxwellian to that of the incoming Gaussian distribution such that

$$\frac{\rho_w}{\rho} = \sqrt{\frac{mP_{yy}}{\rho kT_w}} \tag{23}$$

It can be easily shown that, if the distribution function emitted from the wall has a temperature equal to the temperature normal to the wall of the incoming distribution, the preceding ratio will be one, and Eq. (22) reduces to

$$\mathcal{M}_w(v_x, v_y, v_z) = \frac{\rho}{m(2\pi)^{3/2}(m/kT)^{3/2}} \times \exp\left\{-\left(\frac{m}{2kT}\right)[(v_x - u_{x_w})^2 + v_y^2 + v_z^2]\right\} \tag{24}$$

where T is now the interior fluid temperature.

The requirement that the component of the bulk velocity of the fluid normal to solid walls is zero is a very natural boundary condition for the Gaussian closure and provides one value for the required boundary data. The eigenvalues of the system, however, suggest that two boundary data are required to ensure that the problem is well posed [21,22]. Realizing that, in the equilibrium limit with no accommodation at the wall, the wall shear stress must be zero in order to recover the Euler equations, it seems that a boundary condition for P_{xy} would also be most appropriate. To define the boundary condition for P_{xy}, the appropriate velocity moment of $\mathcal{F}_{Kn}$ given by Eq. (21) must be evaluated and, while not enforced directly as a boundary condition, the full bulk velocity in the Knudsen layer is also required as an intermediate step. It then follows that the following boundary conditions are appropriate for the Gaussian closure in the case of a solid wall extending in the x direction:

$$u_{y_{Kn}} = 0, \qquad u_{x_{Kn}} = (2-\alpha)\left[\frac{u_x}{2} - \frac{P_{xy}}{\sqrt{2\pi\rho P_{yy}}}\right] + \frac{\alpha}{2}\left(\frac{mP_{yy}}{\rho kT_w}\right)^{1/2} u_{x_w} \tag{25}$$

$$P_{xy_{Kn}} = \alpha\left[\frac{P_{xy}}{2} + \sqrt{\frac{\rho P_{yy}}{2\pi}}(u_{x_w} - u_x)\right] \tag{26}$$

with all macroscopic quantities being those of the incoming Gaussian distribution with the exception of u_{x_w} and T_w, which define the Maxwellian $\mathcal{M}_w$ for accommodated particles. It can be seen that Eqs. (25) and (26) allow for velocity slip and finite shear at the wall and recover the correct "no-shear" "full-velocity-slip" limit for specular reflection ($\alpha = 0$).

The preceding solid-wall boundary conditions for the Gaussian closure of a monatomic gas were used for obtaining all of the numerical solutions described herein. An accommodation coefficient of one was used in all cases, except for the final simulation, in which the accommodation coefficient was taken to be zero. For the case of a diatomic gas, an additional zero flux boundary condition was enforced for the rotational energy. Note that additional analysis of solid-wall boundary conditions for the Gaussian closure is given in the recent paper by Khieu et al. [70].

III. Numerical Solution Method

Numerical solution of the Gaussian closure using Godunov-type finite volume schemes have been considered previously by Brown et al. [31,32], Hittinger [67], McDonald and Groth [12,21,22,71], and Lam and Groth [55]. A Godunov-type finite volume scheme with block-based AMR and a treatment for arbitrarily embedded boundaries is proposed here for the numerical solution of the two-dimensional weak conservation form of the moment equations given in Eq. (20). The proposed Godunov-type solution algorithm is implemented on multiblock body-fitted quadrilateral meshes. The scheme allows for solution-directed block-based AMR, and an efficient and highly scalable parallel implementation has been achieved via domain decomposition. A mesh-adjustment scheme is used to perform local alteration of the mesh at embedded boundaries that are not necessarily aligned with the underlying mesh. For moving embedded boundaries, the mesh is restored to its original form and then adjusted to the new location of the embedded boundary at each time step. Key aspects of the parallel AMR scheme for embedded and moving boundaries are now described.

A. Godunov-Type Finite Volume Scheme

By integrating the hyperbolic system of Eq. (20) over a computational cell (i, j) of a multiblock quadrilateral mesh and subsequently applying the divergence theorem, ordinary differential equations prescribing the evolution of the cell-averaged value of the solution vector $\boldsymbol{U}_{i,j}$ can be obtained and written as

$$\frac{\mathrm{d}\boldsymbol{U}_{i,j}}{\mathrm{d}t} = -\frac{1}{A_{i,j}}\sum_{k}[(\boldsymbol{H} - \boldsymbol{w}\boldsymbol{U})\cdot\boldsymbol{n}\Delta\ell]_{i,j,k} - \left(\frac{\boldsymbol{U}\,\mathrm{d}A}{A\,\mathrm{d}t}\right)_{i,j} + \boldsymbol{S}_{i,j} \tag{27}$$

where A_{ij} is the area of the cell; and $\boldsymbol{w}$, $\boldsymbol{n}$, and $\Delta\ell$ are the velocity of, unit normal to, and length of the kth cell face or edge, respectively; and $\boldsymbol{F}_k$ and $\boldsymbol{U}_k$ are the flux dyad and solution at the kth face. The term on the right-hand side of this equation containing the factor $\mathrm{d}A/\mathrm{d}t$ corresponds to the time rate of change of the cell area. This term is approximated by the geometric conservation law that states that the change in cell area is equal to the area swept by the moving surfaces [72]. Given left and right solution vectors, $\boldsymbol{U}_l$ and $\boldsymbol{U}_r$, at each cell interface, the numerical flux is given by

$$(\boldsymbol{H} - \boldsymbol{w}\boldsymbol{U})\cdot\boldsymbol{n} = \mathscr{H}(\boldsymbol{U}_l, \boldsymbol{U}_r, \boldsymbol{w}, \boldsymbol{n}) \tag{28}$$

where the numerical flux $\mathscr{H}$ is calculated by solving a Riemann problem in a frame of reference that is rotated to be aligned with the normal to the face and translated with the edge velocity. The left and right solution states are determined via a least-squares piecewise-linear reconstruction procedure in conjunction with the slope limiter of Barth and Jesperson [73] and Venkatakrishnan [74]. This allows second-order spatial accuracy in smooth regions and first-order accuracy at discontinuities. Roe's approximate solver [75] is used to solve the Riemann problem and evaluate the numerical flux. A suitable Roe linearization of the flux Jacobian of the Gaussian closure for monatomic gases has been determined by Brown et al. [31,32]. A similar linearization has been developed by Hittinger [67] for the diatomic case.

The ordinary differential equations of Eq. (27) are integrated forward in time using a second-order-accurate point-implicit predictor-corrector time-marching scheme [21,22]. In the point-implicit treatment, the hyperbolic fluxes are integrated explicitly, and the collisional source terms are dealt with implicitly. The local nature of the collisional terms allows for an implicit treatment that, following a linearization, involves only the inversion of small local linear systems, which is much easier than the inversion of a large global left-hand side. For time-accurate calculations, the global time step is restricted by the most restrictive Courant–Friedrichs–Lewy (CFL) condition for the fastest moving wave in any cell. For steady-state situations, local time stepping with a local CFL number based on local flow conditions is used to accelerate convergence to the desired time-invariant solution. For all of the steady flow problems considered in the results to follow, a local CFL number of 0.8 was generally used. For the unsteady flow problems, a global CFL number of 0.8 was used. It is recognized that, for steady time-invariant problems, the proposed time-marching scheme is certainly nonoptimal. However, the main thrust of this study is to show the relative robustness of the spatial discretization of the moment equations on the lower-quality meshes resulting from the embedded-boundary treatment. The proposed time-marching scheme is deemed sufficient for such purposes. A more efficient parallel, fully implicit approach has been recently proposed and developed by Lam and Groth [55] for the three-dimensional form of the Gaussian closure based on a Newton–Krylov–Schwarz iterative solution method but is not considered here.

B. Block-Based Adaptive Mesh Refinement on Body-Fitted Mesh

Adaptive mesh refinement has proven to be very effective for treating problems with disparate length scales, providing the required spatial resolution while minimizing memory and storage requirements. Groth and McDonald [12], Sachdev et al. [20], Groth and Northrup [76], Gao and Groth [77,78], and Gao et al. [79] have developed a flexible block-based AMR scheme allowing automatic solution-directed mesh adaptation on multiblock body-fitted (curvilinear) meshes consisting of two-dimensional quadrilateral and three-dimensional hexahedral computational cells. The block-based approach has been shown to enable efficient and scalable parallel implementations for a variety of flow problems, as well as allow local refinement of body-fitted meshes with anisotropic stretching. The latter aids in the treatment of complex flow geometry and flows with thin boundary, shear, and mixing layers and/or discontinuities and shocks. Applications of the block-based AMR scheme have included laminar flames [79,80] and high-pressure soot prediction [81,82], and turbulent non-premixed flames [77–79], as well as turbulent multiphase rocket core flows [20,83] and microscale flows [12,21]. Extensions of the block-based body-fitted AMR approach for embedded boundaries not aligned with the mesh [23] and with an anisotropic refinement strategy [84] are also possible and have been developed. The mesh-adjustment scheme for multiblock body-fitted AMR mesh with embedded boundaries and its application to microscale nonequilibrium flows are the focus here.

Solution of the moment equations by the finite volume method previously outlined yields area-averaged solution quantities defined within quadrilateral computational cells. In the proposed multiblock body-fitted AMR scheme, these cells are embedded in structured body-fitted grid blocks consisting of $N_{\text{cells}} = N_i \times N_j$ cells, where N_i and N_j are integers representing the number of cells in each logical coordinate direction of the block. Mesh adaptation is accomplished by the dividing and coarsening of appropriate solution blocks. The refinement of the mesh is directed by local physics-based refinement criteria (blocks containing high and low values of the chosen criteria are flagged for either refinement or coarsening) as well as by other geometrical criteria related to the needs of accurately resolving embedded/moving boundaries. The AMR algorithm first flags blocks for either refinement or coarsening based on situation-dependent criteria and thresholds. Blocks flagged for refinement are subdivided into four "child" blocks, each of which has the same number of cells in each direction, as did the "parent" block, thus doubling the mesh resolution. If all four child blocks of one parent are later flagged for coarsening, the process can be reversed. Note, however, that no area of the mesh can be made coarser than it was originally. Standard restriction and prolongation operators are used to evaluate the solution on all blocks created by the coarsening and division processes, respectively. Physical boundaries are stored as high-resolution splines; boundary nodes inserted during refinement are placed on these splines. In this way, underresolved boundary geometry will be recovered as the grid is refined.

For the bulk of this study, the mesh-refinement scheme is used primarily to ensure embedded boundaries are well represented by the mesh. Therefore, the refinement criterion used in most cases considered here is simply to flag any block that is crossed by an embedded boundary for refinement. The framework, however, is quite flexible, and it is easy to define a variety of refinement criteria based on simple physical variables (or gradients) or on more sophisticated error estimates or sensitivity analyses.

A hierarchical quadtree data structure is use to keep track of the connectivity between solution blocks, an example of which can be seen in Fig. 1. Solution information is shared between adjacent blocks through the use of "ghost" or "halo" cells. A primary advantage of the quadtree data structure is that it readily permits local mesh refinement. Local modifications to the multiblock mesh can be performed without regridding the entire mesh and recalculating all solution-block connectivity. In this implementation, neighboring blocks are restricted to have a difference in refinement of, at most, one level; this includes corner neighbors. This simplifies the implementation of the prolongation and restriction of ghost-cell information. As well, it makes it easier to maintain the conservation properties of the finite volume scheme. The proper conservation of conserved quantities between blocks of differing refinement levels must be carefully handled such that the overall conservation properties of the finite volume scheme are maintained. If two neighboring blocks are at the same refinement level, there is no issue. Cells in the two blocks will automatically compute the same flux through their shared interface. However, if two neighboring cells are at different refinement levels, special care must be taken. In this case, intercellular

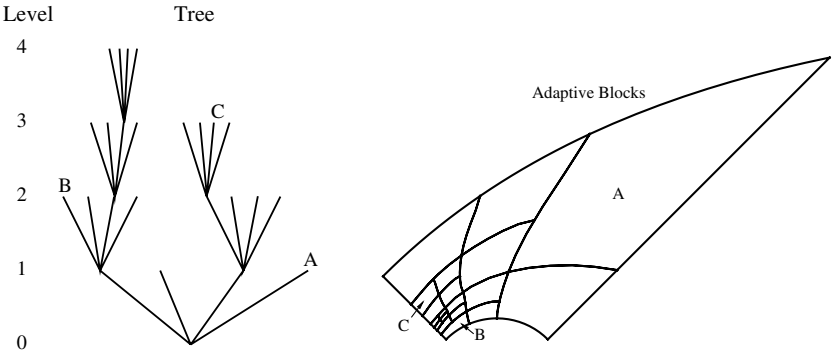

a) Quadtree data structure **b) Multiblock body-fitted grid blocks**

Fig. 1 Block-based AMR scheme showing four levels of refinement.

fluxes computed on the more refined grid are taken to be more accurate and replace fluxes computed along the shared edge of the coarser block. Each cell along the edge of the coarser block will share an edge with two cells from the more refined block, and the flux through the shared edge is simply the sum of the fluxes computed for the more refined pair of cells.

C. Parallel Implementation

By design, the multiblock body-fitted AMR scheme is well suited to parallel implementation on distributed-memory multiprocessor architectures via domain decomposition. Grid blocks are simply distributed equally among the available processors, with more than one block permitted on each processor. Due to the similar nature of the grid blocks, an efficient decomposition can be readily achieved, leading to high parallel efficiency and scalability. Every time AMR is applied, the solution blocks are redistributed to ensure optimal load balancing. If the resulting number of blocks is not evenly divisible by the number of processors, there can be an imbalance of, at most, one block per processor. Parallel implementation of the block-based AMR scheme has been carried out using the message passing interface library [85,86]. Message passing of information between processors is largely limited to the asynchronous communication of ghost-cell solution values.

D. Mesh-Adjustment Scheme

To add greater flexibility for the treatment of microscale flows with complex flow geometries, the preceding finite volume scheme has been combined with the mesh-adjustment scheme proposed recently by Sachdev and Groth [23,24]. The mesh-adjustment scheme provides an automated treatment for both fixed and moving non-grid-aligned boundaries embedded in a body-fitted multiblock mesh. Similar in nature to the Cartesian-cut-cell methods developed by Bayyuk et al. [87] and Murman et al. [88], this scheme allows for the nodes of an underlying body-fitted mesh to be adjusted so as to coincide with the embedded boundary. By making only local alterations to the grid, this scheme enables the solution of unsteady flows involving moving boundaries or for steady flow problems involving stationary boundaries that are not necessarily aligned with the mesh while preserving the structured nature of the blocks. It also seems to automatically avoid the creation of small cut cells, which are often generated by traditional cut-cell approaches, without the need for any special treatment, such as the merging of small cut cells into larger neighbors [23,24]. In addition, the mesh-adjustment algorithm is fully compatible with block-based AMR and parallel implementation via domain decomposition used in the finite volume scheme previously described. A brief summary of the mesh-adjustment scheme is given in what follows. Refer to the paper by Sachdev and Groth [23] and the thesis by Sachdev [24] for further details.

Mesh adjustment is carried out in several steps, as illustrated in Fig. 2. First, a pre-mesh-adjustment flagging is applied in order to identify cells that may require adjustment. The nodal locations of each cell are compared to bounding boxes that are constructed for each interface; a cell is flagged to be active if all four of its nodes lie outside all bounding boxes. Next, if the cell is partially or entirely contained in a bounding box, intersections between the edges of the cell and each boundary are sought. If no intersections exist, a ray-tracing algorithm is employed to determine if the cell is entirely inside or outside of the boundaries. This ray tracing simply entails counting the number of intersections between the line segments comprising the embedded boundary and a line segment connecting the cell centroid to a reference point known to lie within the boundary. An odd number of intersections indicates that the cell is outside of the interface. These cells are used during the solution of the moment equations and are tagged as "active" cells. Conversely, an even number of intersections indicates that the cell is inside the interface and can be tagged as "inactive". The latter are not used in the solution of the moment equations. All cells that have not been deemed active or inactive are labeled as "unknown".

The first mesh-adjustment step involves identifying sharp corners in the interfaces. The unknown cell that contains each sharp corner is identified, and its nearest node is moved onto the corner. Once a

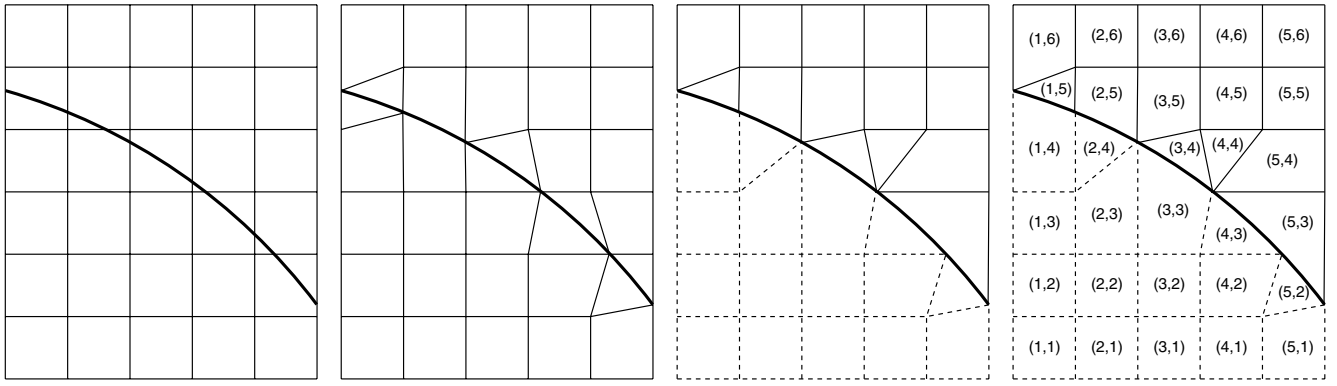

a) Initial mesh **b) Primary adjustment** **c) Secondary adjustment** **d) Final structured mesh**

Fig. 2 Mesh-adjustment algorithm.

node has been adjusted to lie on a boundary, it is tagged as "aligned". For the remaining unknown cells, the nodes nearest to the boundary are moved to the closest point of intersection between the interface and the mesh lines, as shown in Fig. 2b. This step is performed twice to increase the robustness of the procedure, particularly on course meshes when a cell face can have multiple intersections with a boundary. Again, nodes that have been moved are tagged as aligned. This movement will leave cells that are bisected diagonally by the boundary. To account for this, the secondary step involves moving the nearest not-yet-aligned node of bisected cells so that it also lies on the boundary. This step will produce triangular cells, as depicted in Fig. 2c. All triangular cells are simply treated as degenerate quadrilaterals with two coincident nodes. The final step in the mesh-adjustment algorithm involves using the same ray-tracing technique previously mentioned to determine which of the unknown cells are active and which are inactive. The resulting mesh remains structured and does not result in neighboring cells of radically different sizes.

The current implementation also allows for moving embedded boundaries for which the motion can be prescribed either explicitly or through a level-set method [89,90]. Boundary locations are computed at each time step, and the mesh is readjusted. The velocity of the embedded boundary is accounted for during the calculation of the solution flux and the effect of the rate of change of cell area is included as a source term [see Eq. (27)]. To avoid excessive tangling, the mesh is first returned to an unadjusted state and then readjusted. Cells near the boundary will therefore change shape, and previously active cells may become inactive, or vice versa. Solution content is supplied to newly activated cells and removed from newly deactivated cells through a redistribution algorithm designed to ensure the conservation properties of the finite volume scheme. The solution content of a newly deactivated cell is area averaged into neighboring active cells. The solution content of a newly activated cell is determined by taking the area-weighted average of the parts of the active cells from the previously adjusted mesh that intersects with the newly activated cell. A more detailed explanation of the mesh-adjustment scheme and solution redistribution algorithm is provided in the paper by Sachdev and Groth [23] and the thesis by Sachdev [24]. This redistribution algorithm is akin to the projection stage of a finite volume scheme in which cell-averaged solution values are determined.

Though this implementation is tailored for two-dimensional situations, extension to three-dimensional structured meshes is certainly possible. In a three-dimensional version, cells intersected by an embedded surface would be identified and flagged for adjustment. Next, the nearest nodes would be moved along grid lines to a point intersected by the boundary. The number of ways in which a hexahedral cell can be intersected by a boundary is larger than that for two-dimensional quadrilaterals; however, it should be possible to implement the logic required to move additional cell nodes onto the boundary such that no bisected cells result from the boundary treatment. A similar ray-tracing algorithm can be used to find which points are within an embedded boundary.

IV. Numerical Results

To verify and explore the potential of the proposed approach for predicting nonequilibrium microchannel flows, several flow problems are now considered. The accuracy of the proposed finite volume spatial discretization procedure and AMR algorithm with embedded-boundary treatment is first assessed for a problem for which an analytical solution has been determined by using the method of manufactured solutions. Subsonic, laminar boundary-layer flow over a flat plate is then examined to demonstrate that the embedded-boundary treatment and hyperbolic nature of the governing equations will yield smooth predictions of the frictional drag forces acting on the plate; traditional cut-cell-type approaches combined with the Navier–Stokes equations have been shown to produce large oscillations in viscous drag predictions [29]. Subsequently, subsonic, laminar, Couette flow is studied for a range of Knudsen numbers. The aim in this case is to show that the combination of the Gaussian closure with appropriate boundary conditions can describe the full range of flows from the well-known continuum regime at low Knudsen numbers, through the transition regime, and on to the free-molecular regime at high Knudsen numbers. It is demonstrated that the solutions are equally well predicted by meshes that are aligned and nonaligned to the plates. Next, subsonic laminar flow past a circular cylinder is considered. This case is considered to illustrate the applicability of the Gaussian closure and proposed solution scheme to transition-regime flows. Previous investigations using body-fitted meshes have shown good agreement with experimental results [21], and it is shown here that results of equivalent accuracy can be achieved with the proposed embedded-boundary treatment. To show the ease with which complicated geometries including multiple stationary and moving embedded boundaries can be treated, a microscale channel flow with a more complicated moving geometry is also considered for both continuum and nonequilibrium flows. A final demonstration of the capabilities of the proposed modeling and solution methods is provided by a NACA 0012 airfoil undergoing a prescribed oscillatory pitching motion. For this case, the treatment for embedded moving boundaries is combined with solution-directed AMR, and comparisons are made with available experimental data. For all of the cases considered, values of the mean free path λ used in defining the Knudsen number were determined using the expression for hard-sphere collisional processes given by Bird [5].

All of the two-dimensional computations were performed on a high-performance parallel cluster consisting of 3780 Intel Xeon E5540 (2.53 GHz) nodes with eight CPU cores and 16 GB of RAM per node. The cluster is connected with a high-speed low-latency InfiniBand switched fabric communications link. The steady-state flat-plate flow cases on the finer mesh required about 2–3 h of wall-clock time using 96 processor cores. Similarly, the steady-state cylinder flow cases necessitated approximately 1 h on 48 cores. The unsteady airfoil case required about 300 h on 48 cores. These timings may seem high; however, this work was done using a research code and, as such, there are a number of inefficiencies in the implementation that would not be present in a production code. Steady-state simulations were deemed to be converged once the residual of x-direction momentum density had been reduced by at least six orders of magnitude.

A. Manufactured Solution Between Two Concentric Cylinders

The proposed finite volume spatial discretization procedure, semi-implicit time-marching scheme, and AMR algorithm with adjusted mesh and embedded-boundary treatment are nominally second-order accurate with discretization errors of $\mathcal{O}(\Delta x^2, \Delta t^2)$, where Δx and Δt are the spatial and temporal discretization step sizes. Although the second-order spatial accuracy of the finite volume scheme and AMR method with mesh adjustment have been previously verified by Sachdev and Groth [23,24] for a related nonlinear hyperbolic system of conservation laws, with the Euler equations corresponding to the Maxwellian closure, it is important here to establish that a similar accuracy can be achieved for the moment equations of the Gaussian closure before proceeding to the application of the methodology to more practical flow problems. As there are no practical situations for which analytical solutions to the Gaussian moment equations are known, the method of manufactured solutions is used to construct such a solution for which the formal accuracy of the proposed scheme can be assessed.

The method of manufactured solutions is a rather simple procedure that allows analytical solutions to be constructed for the PDEs of interest by slightly modifying the equations through the addition of source terms. This can be done for the Gaussian closure by prescribing a solution $\tilde{\boldsymbol{U}}$, the desired analytical result, and determining analytically the associated solution residual vector as defined by Eq. (20) and given by

$$\tilde{\boldsymbol{R}} = \frac{\partial \tilde{\boldsymbol{U}}}{\partial t} + \frac{\partial \boldsymbol{F}(\tilde{\boldsymbol{U}})}{\partial x} + \frac{\partial \boldsymbol{G}(\tilde{\boldsymbol{U}})}{\partial y} - \boldsymbol{S}(\tilde{\boldsymbol{U}}) \tag{29}$$

This residual is then added as a source to the original moment equations of Eq. (20), such that the prescribed solution $\tilde{\boldsymbol{U}}$ is in fact the analytical solution to the modified moment equations given by

$$\frac{\partial \boldsymbol{U}}{\partial t} + \frac{\partial \boldsymbol{F}}{\partial x} + \frac{\partial \boldsymbol{G}}{\partial y} = \boldsymbol{S} + \tilde{\boldsymbol{R}} \tag{30}$$

Discretization errors of the proposed numerical solution method can then be assessed by direct comparison of predicted solutions to the analytical result, $\tilde{\boldsymbol{U}}$.

Here, in order to assess the spatial accuracy of the finite volume scheme and AMR method with embedded-boundary treatment, predictions for a time-invariant manufactured solution for the Gaussian moment closure of monatomic gas on a domain between two concentric cylinders are considered. The prescribed solution is this case was chosen to be

$$\begin{aligned} \rho &= 2 + \sin(x + y), \\ u_x &= \cos(x + y), \\ u_y &= \sin(x - y), \\ P_{xx} &= 3 - \sin(x + y), \\ P_{xy} &= \sin(y - x), \\ P_{yy} &= 3 + \cos(x + y), \\ P_{zz} &= 3 + \cos(-x - y) \end{aligned} \tag{31}$$

The offsets in the density and normal components of the pressure tensor ensure that the Gaussian solution remains physically realizable everywhere. The problem domain was chosen to be an annulus lying between cylinders of radii of 0.1 and 0.5 m. To ensure that the hyperbolic and relaxation parts of the system are both of similar magnitude and impact, the relaxation time was taken to be $\tau = 1$ s.

Adjusted computational grids were generated for this problem by imposing two embedded circular boundaries on to regular Cartesian grids of varying resolution. An initial Cartesian grid was considered containing 32×32 cells, 200 of which are active after application of the embedded-boundary treatment. Additional grids were then generated by consecutively doubling the resolution of the initial Cartesian mesh in each direction. This produced a sequence of four adjusted meshes between the two circular embedded boundaries having 200, 780, 3104, and 12,371 active cells, respectively. The four adjusted computational grids are depicted in Fig. 3.

Predicted solutions for the time-invariant manufactured solution on the four adjusted meshes were obtained using the numerical scheme previously outlined. The exact analytical solution was prescribed on the domain boundaries, and the numerical solution was advanced in time until converged steady-state results were achieved. The corresponding error norms for the predicted solutions on the four adjusted meshes are shown in Fig. 4. L_1, L_2, and L_∞ norms of the difference between the analytical and numerical solutions are all given in the figure as a function of the nominal mesh density as represented by the square root of the number of active cells in each mesh. The average slopes for the L_1, L_2, and L_∞ error norms are -1.97, -2.03, and -1.99, respectively. It is evident from these result

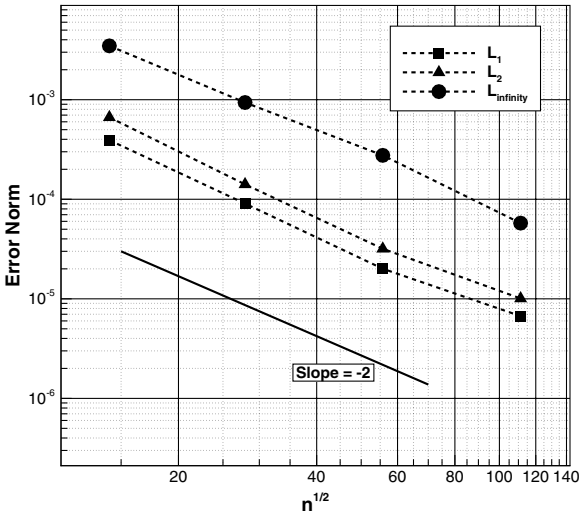

Fig. 4 L_1, L_2, and L_∞ error norms for the manufactured-solution problem.

that the spatial accuracy of the scheme is indeed second order, even for the adjusted meshes of degraded quality caused by the embedded boundaries. Similar findings were obtained by Sachdev and Groth [23,24] for the Euler equations of inviscid compressible gas dynamics.

B. Subsonic Laminar Flat-Plate Boundary-Layer Flow

Subsonic boundary-layer airflow past a flat plate is considered. For this diatomic gas case, the freestream Mach and Reynolds numbers are $Ma = 0.2$ and $Re = 2,000$, respectively, and the Knudsen number is 1.5×10^{-4}, which indicates that the flow is laminar and in the continuum regime. Results for two computational meshes are considered: one aligned with, or at 0 deg to, the plate; and a second mesh at 30 deg to the plate. Both meshes initially consisted of one 16×16 Cartesian square block centered on the origin of the x and y axes. A boundary representing the flat plate was embedded in the block. This boundary is a line that is coincident with the x axis and passes through the origin. For $x < 0$, inviscid slip or reflection boundary conditions were used, whereas for $x > 0$, no-slip solid-wall boundary conditions with full accommodation were used. To reduce the influence of the outflow boundary on the solution, the computational domain and plate extended approximately 20% further than the plate length of interest and the solution at all other boundaries is made equal to be a corresponding Navier–Stokes Blasius solution. The computational grid was then subjected to six or eight mesh refinements such that, at each level of refinement, any block crossed by the boundary was refined. The result was a mesh comprising 376 blocks and 48,128 active cells for the 0 deg case and 508 blocks and 65,024 active cells for the 30 deg case when six levels of refinement were applied. For eight levels of refinement, 764 active blocks and 195,584 active cells for the 0 deg case and 1271 active blocks and 276,992 active cells for the 30 deg case were used. Sections of both the aligned and nonaligned meshes are provided in Fig. 5. The somewhat larger number of cells in the nonaligned case is a result of the fact that, at

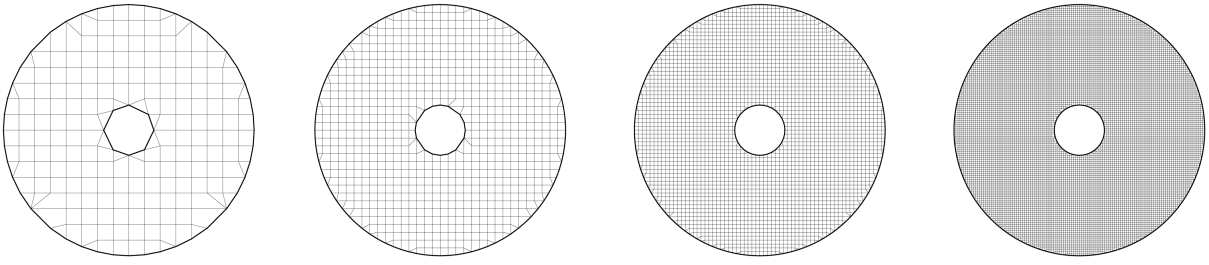

a) n = 200 **b) n = 780** **c) n = 3104** **d) n = 12,371**

Fig. 3 Sequence of adjusted meshes with embedded circular boundaries.

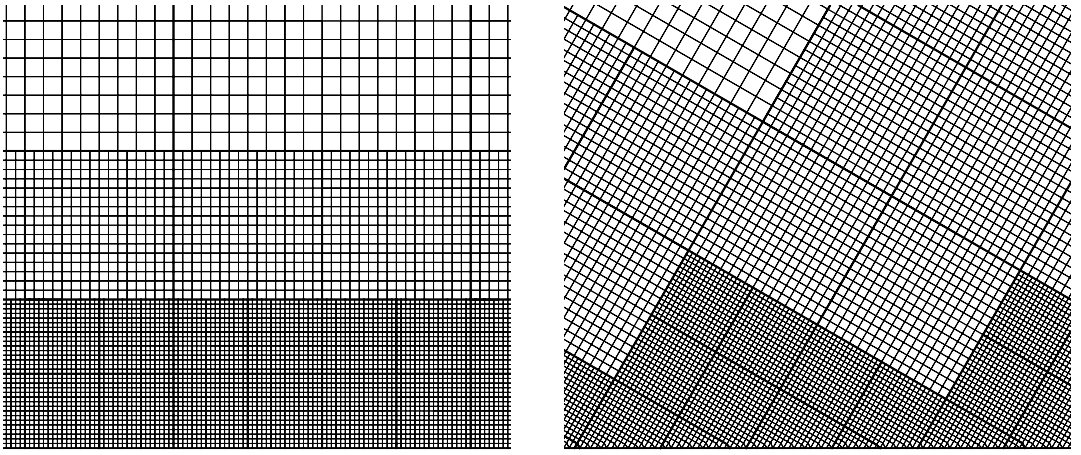

a) Aligned mesh at 0° to plate **b) Nonaligned mesh at 30° to plate**

Fig. 5 Computational grids used in the numerical prediction of laminar boundary-layer flow.

30 deg, the interface crosses more blocks, which will be flagged for refinement; nevertheless, the smallest cells are the same size for both grid angles.

With eight levels of refinement, the Knudsen number based on the cell size varied from 4.1×10^{-3} to 0.26. With a local CFL number of 0.8, the semi-implicit time-marching scheme was able to effectively deal with any numerical stiffness associated with interparticle collisions arising in the larger cells for this continuum flow problem.

The numerical predictions of the profile of the local skin-friction coefficient C_f along the length of the plate obtained using the Gaussian closure for the laminar boundary-layer flow previously described are shown in Fig. 6, along with comparisons to the classical boundary-layer results of Blasius [91]. The results of the figure show that there is excellent agreement between the skin-friction coefficient profiles predicted by the moment closure and the Blasius solution. Furthermore, the two sets of computed results for six and eight levels of mesh refinement on both the aligned and nonaligned computational grids, shown in the close-up view, demonstrate the convergence of the Gaussian closure solutions, as the grid is refined as well as the relative independence of the solutions to grid orientation with the embedded mesh treatment. Clearly, the Blasius solution is recovered as the mesh is refined for both aligned and nonaligned cases, and the two results are virtually identical with eight levels of mesh refinement.

It is also important to note that the results of Fig. 6 indicate that there are no oscillations present in the Gaussian-closure predictions of the skin-friction coefficient on the nonaligned computational grids. These smooth profiles are in definite contrast to previous results obtained by Sachdev and Groth using the Navier–Stokes equations [23,24]. Figure 7a shows typical results for the prediction of the skin-friction coefficient for flow past a flat plate angled at 30 deg to the grid obtained using the standard Navier–Stokes model. For these Navier–Stokes solutions, the elliptic diffusion terms through cell interfaces were discretized based on a Green–Gauss integration around a diamond path created by the points describing the cell centers of the neighboring cells and the nodes defining the interface. This technique was proposed by Coirier and Powell [30]. The exact details of the current implementation are available in the paper by Sachdev and Groth [23] and thesis by Sachdev [24]. The identical mesh-adjustment scheme with both six and eight levels of refinement was again used. The oscillations present in the predicted skin-friction profile of this figure are entirely due to the necessity of evaluating second derivatives in the solution of the Navier–Stokes equations and the sensitivity of numerical treatments for these higher-order derivatives to grid irregularities caused by the embedded boundary. As is evident from Fig. 7b, the oscillations in the predicted skin-friction coefficient are directly related to local modifications to the mesh caused by the embedded boundary. There is a systematic jump in the skin-friction profile whenever the row of cells intersected by the boundary changes. The results also show that it is not necessarily simply a matter of further refinement of the mesh in order to yield improved results for the Navier–Stokes equations. The

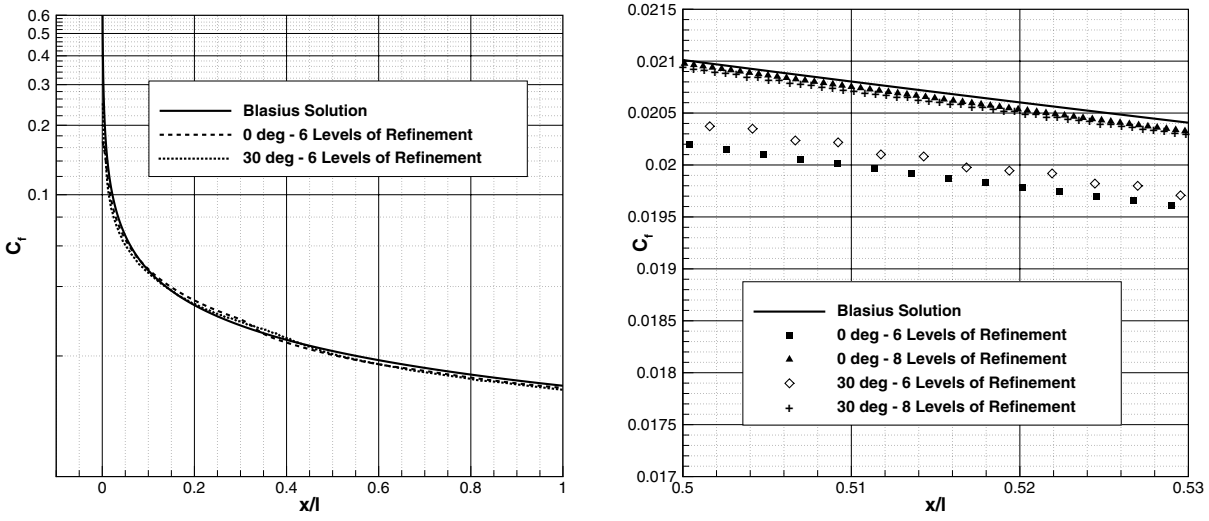

a) Skin-friction coefficient **b) Close-up view**

Fig. 6 Numerical prediction of skin-friction coefficient for flow past a flat plate

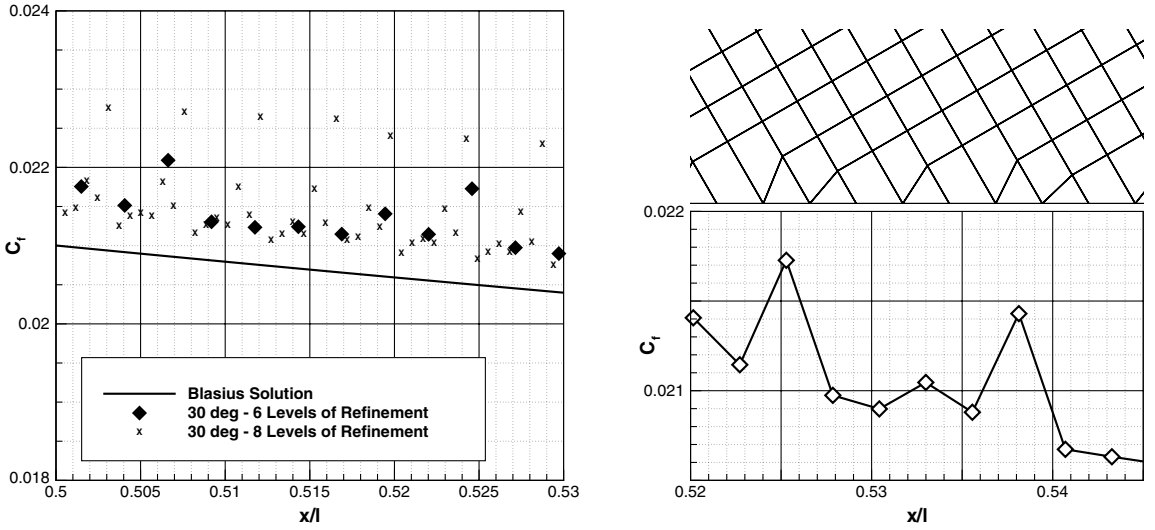

a) Skin-friction coefficient **b) Influence of mesh**

Fig. 7 Skin-friction coefficient for boundary-layer, computed using the Navier–Stokes equations.

Navier–Stokes solution obtained here for the more refined mesh are somewhat worse and exhibit even larger solution jumps. Similar oscillations in the predicted skin-friction coefficients, with even larger and far more deleterious excursions, were observed in the AMR solutions of Coirier [29] and Coirier and Powell [30] using a cut-cell approach.

Additional evidence of grid convergence for the flat-plate boundary-layer flow is demonstrated in Fig. 8. Here, solutions to the boundary-layer flow were again computed on sequences of meshes that were constructed either with uniform mesh spacing or with AMR. Results for both aligned (0 deg) and nonaligned (30 deg) grids were again considered. The coefficient of total drag C_D was then computed from the integrated predicted skin-friction profiles in each case and plotted as a function of the mesh resolution. It is evident from the figure that the predicted drag on each sequence of grids is convergent and that the solutions on each sequence are converging to the same result ($C_D \approx 0.028$). Although the converged value for the drag coefficient predicted by the Gaussian closure is slightly less than the value of 0.0297 predicted by the Blasius solution, this is expected because the Blasius solution yields a skin-friction coefficient that approaches infinity at the leading edge, whereas the Gaussian closure does not; therefore, even though the solutions to the moment equations agree well with the Blasius solution further along the plate, they tend to predict a somewhat lower drag near the plate leading edge.

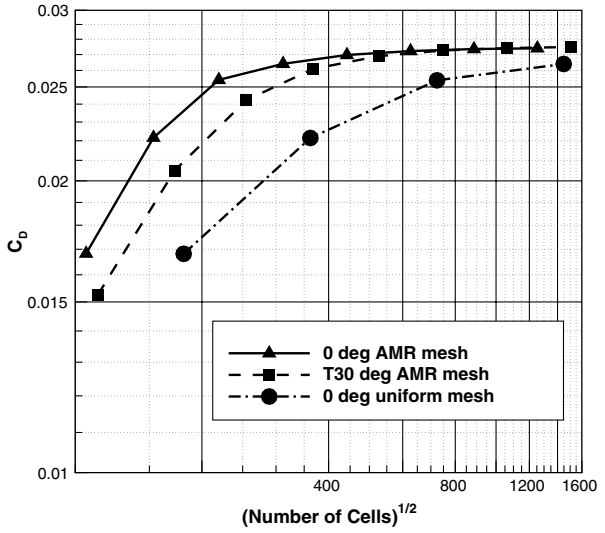

Fig. 8 Predicted coefficient of drag for boundary-layer flow with varying mesh resolution.

Figure 8 also provides a good illustration of the computational advantages provided by the proposed AMR scheme. It can be seen that the solutions obtained using AMR achieve a given level of accuracy using only a fraction of the number of cells required to obtain the same level of accuracy on a uniform mesh. Obviously in this situation, mesh point and grid line clustering could be used to concentrate cells near the boundary to obtain similarly accurate results to those of the AMR mesh. However, in more complicated situations, it is not always clear where enhanced spatial resolution is needed and mesh clustering and/or stretching may not be effective. Also, if the domain boundaries are moving or evolving during the simulation, areas requiring increased resolution will also move and change over time. Adaptive mesh refinement is especially useful in these situations.

C. Subsonic Laminar Couette Flow

The second problem considered is the one of Couette flow for a gas spanning a variety of flow regimes. The current investigation comprises two infinite-span plates separated by a fluid-filled gap. The two plates are translating in opposite directions with a speed of $u_p = 30$ m/s. The gap between the plates is filled with argon at a temperature of $T = 288$ K and standard pressure; the diatomic extension to the Gaussian closure is therefore not used for this case. The gap width d was varied such that a range of flow Knudsen numbers, $Kn = \lambda/d$, were considered. Again, two embedded meshes are considered, one aligned at 0 deg to the plates and one at 30 deg to the plates. The original unadjusted mesh in each case comprised 10,240 cells; however, many of these cells were inactive. The number of active cells for the aligned (0 deg) mesh was 2560 and, for the nonaligned (30 deg) mesh, there were 3956 active cells. The topologies of the two computational meshes used in the Couette flow study are given in Fig. 9. For this problem, the Knudsen number based on the cell size depended on the flow Knudsen number considered. The cell Knudsen number was about 0.68 for a flow Knudsen number of $Kn = 0.01$ and was about 680 for the $Kn = 10$ case. Therefore, even for the $Kn = 0.01$ case and with a local CFL number of 0.8, the source terms associated with particle collision processes did not introduce significant numerical stiffness and collision timescales were essentially resolved. A value of the cell Knudsen number near unity, even for near-continuum situations with small flow Knudsen numbers, indicates that the timescales for transport and collisional effects are similar in magnitude.

Boundary conditions for the solid walls of the two plates were applied as previously described. At the remaining two boundaries, the velocity and the shear component of the pressure tensor were extrapolated, whereas all other flow properties where held fixed. This situation is particularly well suited for the Gaussian moment closure,

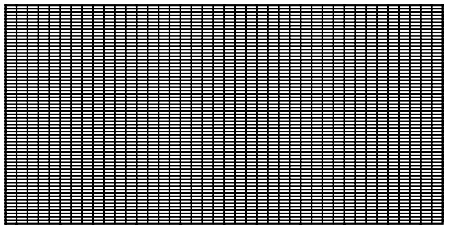

a) Aligned mesh at 0° to upper and lower plates

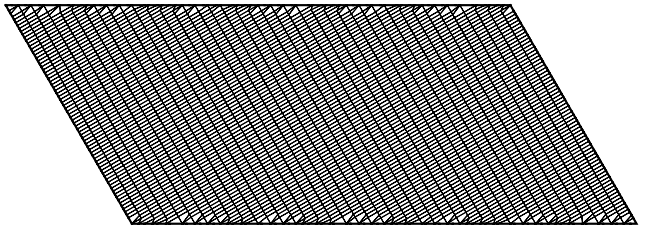

b) Nonaligned mesh at 30° to upper and lower plates

Fig. 9 Grids used in subsonic laminar Couette flow computations.

as the continuum and free-molecular exact solutions do not have heat transfer. The lack of heat transfer in the moment equations should therefore not lead to significant solution errors in either of these regimes. The Couette flow problem is therefore a good test case to demonstrate the validity of the solid-wall boundary treatment across the full range of Knudsen numbers.

Figure 10 shows both the predicted normalized flow velocity at the wall, u/u_p, and normalized shear stress, $\tau_{xy}/\rho u_p\sqrt{2kT/\pi m}$, for the Couette problem as a function of Knudsen number. Values for the fluid velocity at the wall shown in Fig. 10 were evaluated by taking the average along each plate, and values for the fluid shear were evaluated by taking the average over the entire domain. The results show that the Gaussian closure, combined with the Knudsen-layer analysis for the solid boundary, is able to reproduce the correct results in both the continuum (Navier–Stokes) regime, where there is no slip between the fluid and the wall; and the free-molecular regime, where there is perfect slip. In addition, it provides solutions that effectively transition from the continuum result to the free-molecular-flow values in a manner that is in very good agreement with an approximate analytical solution developed by Lees [92]. Lastly, the numerical predictions are essentially independent of the computational mesh used (i.e., the aligned and nonaligned mesh results are almost indistinguishable) and further demonstrate the high accuracy that can be achieved using the Gaussian closure coupled with the embedded-mesh algorithm.

D. Subsonic Laminar Flow Past a Circular Cylinder

As a next case, subsonic airflow past a circular cylinder is considered. Experimental results at low-speed and high-Knudsen numbers have been previously obtained by Coudeville et al. [93] for this case. The application of the Gaussian closure to this case was previously considered by McDonald and Groth using body-fitted meshes [21] for two speed ratios, $S = 0.027$ and $S = 0.107$, and a wide range of Knudsen numbers in the continuum and transition regimes. The speed ratio S is the ratio of the mean flow speed to the most likely random component of a gas particle's velocity; it differs from the Mach number by a factor of $\sqrt{2/\gamma}$. These previous numerical results are reproduced in Fig. 11, where the predictions of the coefficient of drag C_d for the cylinder flow are compared to the experimental results due to Coudeville et al. [93] and an approximate analytical expression due to Patterson [94].

To demonstrate that the present embedded-mesh treatment can recover the drag results for the circular cylinder previously described with virtually equal accuracy to those obtained with a body-fitted mesh, values for the coefficient of drag were recomputed using the Gaussian closure and embedded-mesh approach for a range of Knudsen numbers at the higher speed ratio of $S = 0.107$. All of the computations were again conducted on a square-shaped Cartesian mesh that initially contained one 16×16 block with an embedded circular cylinder. For most cases, the square domain had a dimension that was 125 times the cylinder radius, and the far-field solution was assigned the freestream values. This mesh was then refined 10 times in order to capture the boundary, resulting in a mesh of 556 blocks and 112,936 active cells, as seen in Fig. 12. The cylinder diameter d was varied such that a range of flow Knudsen numbers, $Kn = \lambda/d$, were considered. As the cylinder radius decreases and Knudsen number increases, the relative distance to which the flow is disturbed by the cylinder boundary layer also increases. Thus, in order to eliminate the effects of the far-field boundary on the numerical solution, the size of the initial grid had to be enlarged for the $Kn = 0.5$ and $Kn = 1$ cases. Additional levels of mesh refinement were then used in order to maintain the resolution at the inner boundary. As with the Couette flow problem, the Knudsen number based on the cell size depended on the flow Knudsen number of interest. The cell Knudsen number varied from about 0.020 to 2.6 for a flow Knudsen number of $Kn = 0.01$ and ranged from 0.2 to 105 for the $Kn = 1$ case. As for the flat-plate boundary-layer flow, the proposed semi-implicit time-marching scheme with a local CFL number of 0.8 was able to cope with the numerical stiffness associated with interparticle collisions arising in the larger cells of the near-continuum regime cases.

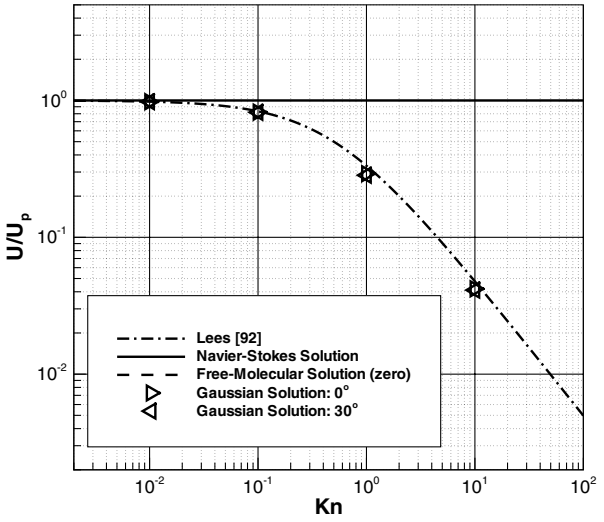

a) Flow velocity at wall

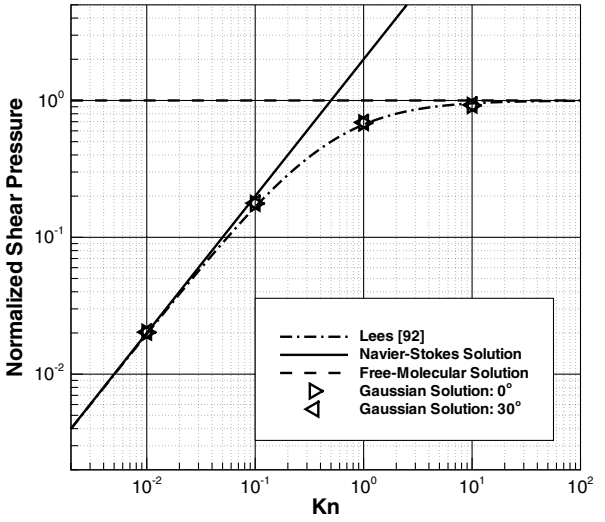

b) Shear stress at wall

Fig. 10 Numerical predictions of normalized velocity and shear stress for Couette flow.

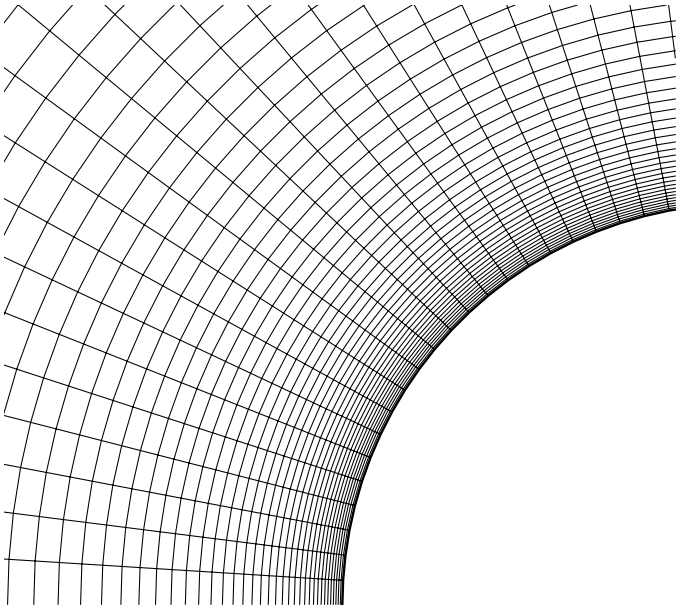

a) Body-fitted computational mesh

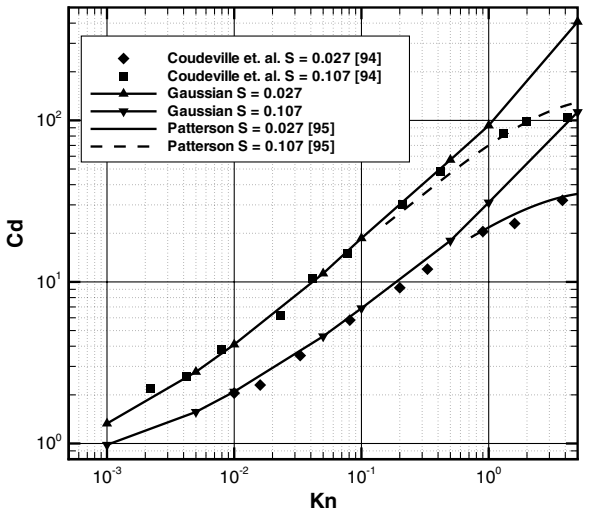

b) Coeciffient of drag

Fig. 11 Predicted drag for airflow past a circular cylinder with body-fitted mesh.

The resulting embedded AMR mesh predictions of the coefficients of drag are shown in Fig. 12. The embedded-mesh results are compared the Gaussian-closure solutions obtained previously using a body-fitted mesh, as well as to the experimental results collected by Coudeville et al. [93]. It is quite apparent that agreement between the experimental results and the values predicted by the Gaussian closure are equally accurate when the embedded-boundary treatment is used. There does, however, appear to be a growing discrepancy between both sets of computational results and the experimental data as the Knudsen number approaches unity. This is likely due to the fact that the Gaussian closure does not account for the large nonequilibrium and heat transfer effects that are present under more highly rarefied conditions.

E. Subsonic Laminar Channel Flow with Moving Boundaries

In previous work, Coirier [29] explored subsonic laminar flow of air through a branched channel containing three rows of pin cooling fins (14 pins in total) using a Cartesian-cut-cell approach. The geometry of the problem was originally designed so as to loosely model the flow within turbine blades. It involves a channel through which fully developed flow enters. The upstream solution flow was taken to be fully developed pipe flow with an average Mach number of $Ma = 0.1$. At the two outflows, a constant-pressure boundary condition was used, in which all other flow variables are extrapolated. The channel contains a branch with the three rows of cooling pins. The pin obstructions produce flow resistance and losses, and they cause a portion of the flow to be redirected through a secondary channel. A similar case is considered here, except two of the three rows of the pins are now assumed to move relative to the center stationary row with a prescribed oscillatory motion (i.e., 10 pins have a prescribed oscillatory motion). This case has been included here to show how easily the current embedded-boundary treatment can be used for cases with numerous embedded boundaries (i.e., one for each pin as well as the channel boundaries), some of which are moving with respect to the frame of the computational mesh.

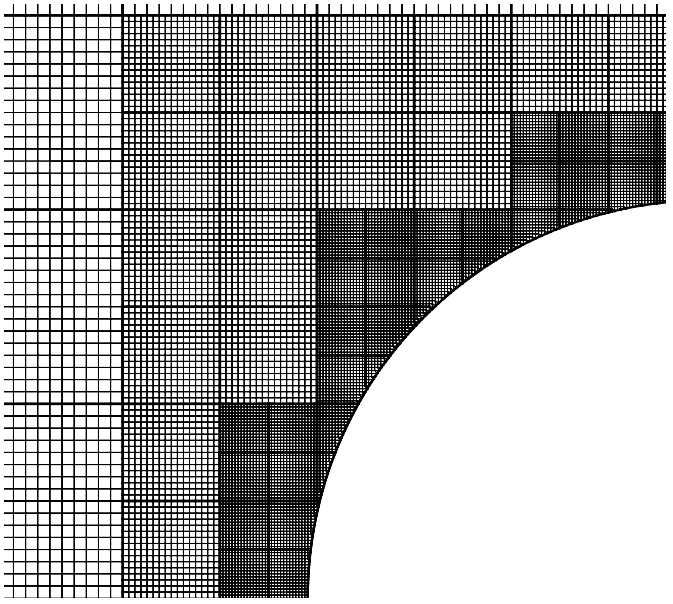

a) Embedded computational mesh

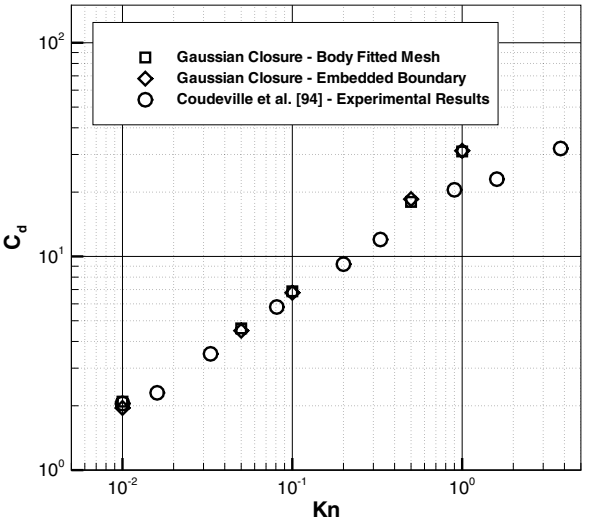

b) Coeciffient of drag

Fig. 12 Predicted drag for airflow past a circular cylinder with embedded-boundary mesh.

The computational grid used for the branched-channel problem is shown in Fig. 13. A close-up view of the area surrounding the 14 cooling pins at three different instances in time is shown in Fig. 14. The latter shows the initial as well as the extremes of the pin row motion. Two flow Knudsen numbers (based on pin diameter) were examined for this case: $Kn = 7 \times 10^{-6}$ (continuum flow regime) and $Kn = 7 \times 10^{-2}$ (transitional flow regime). For both cases, the simulation was originally run to steady state with the pins held stationary, and then the oscillatory motion of the pins was initiated. For the continuum-regime solution, the steady-state result was found to be in good qualitative agreement with Coirier's solution [29] and possessed similar flowfield and recirculation patterns.

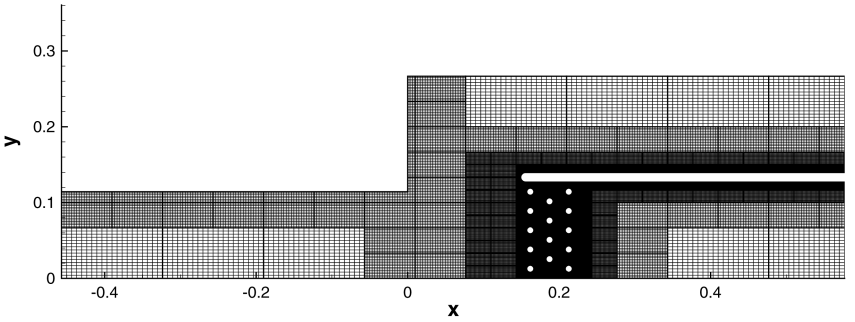

Fig. 13 Multiblock, AMR, grid with embedded-boundary used in subsonic branched-channel simulation.

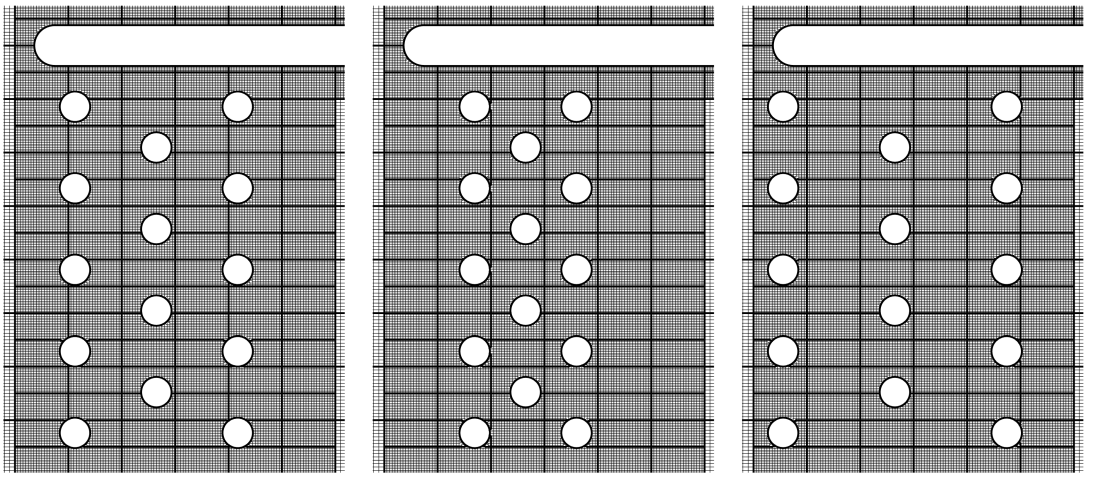

a) Initial positions **b) Minimum separation** **c) Maximum separation**

Fig. 14 Close-up view of mesh around embedded pins for branched-channel simulation.

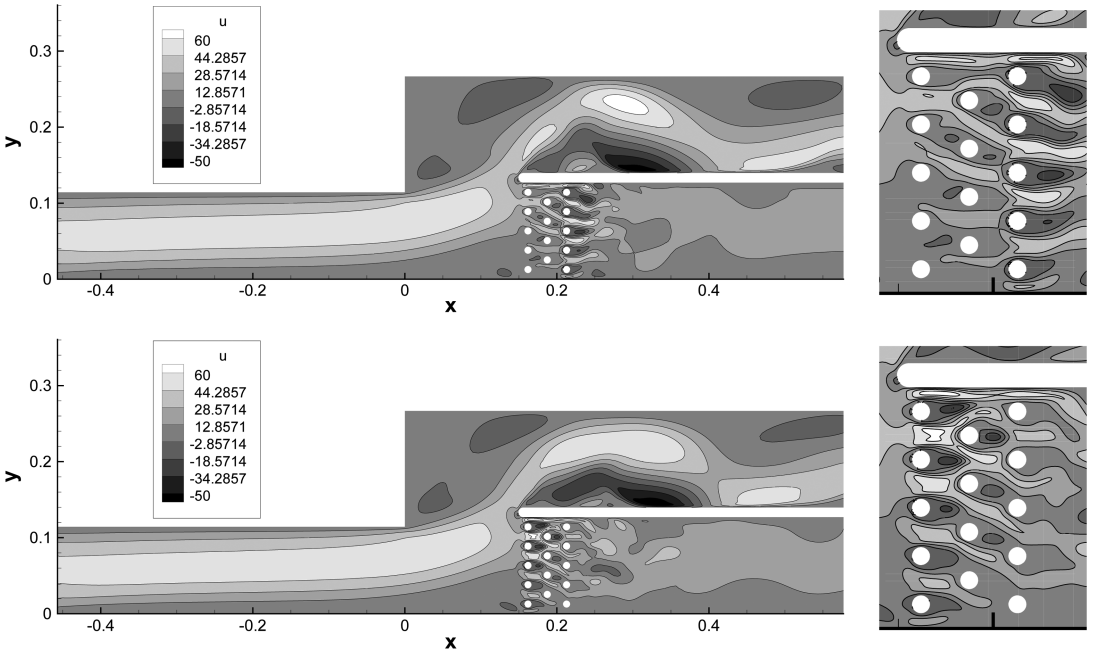

Fig. 15 Branched-channel flow prediction for $Kn = 7 \times 10^{-6}$; $t = 10$ ms (top); $t = 15$ ms (bottom).

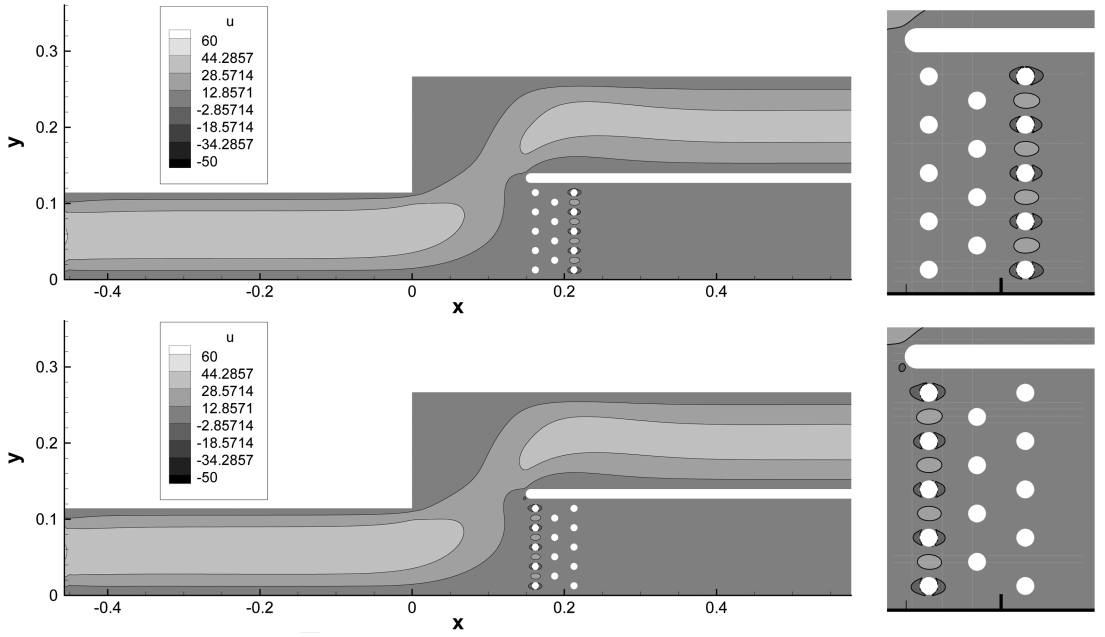

Fig. 16 Branched-channel flow prediction for $Kn = 7 \times 10^{-2}$; $t = 10$ ms (top); $t = 15$ ms (bottom).

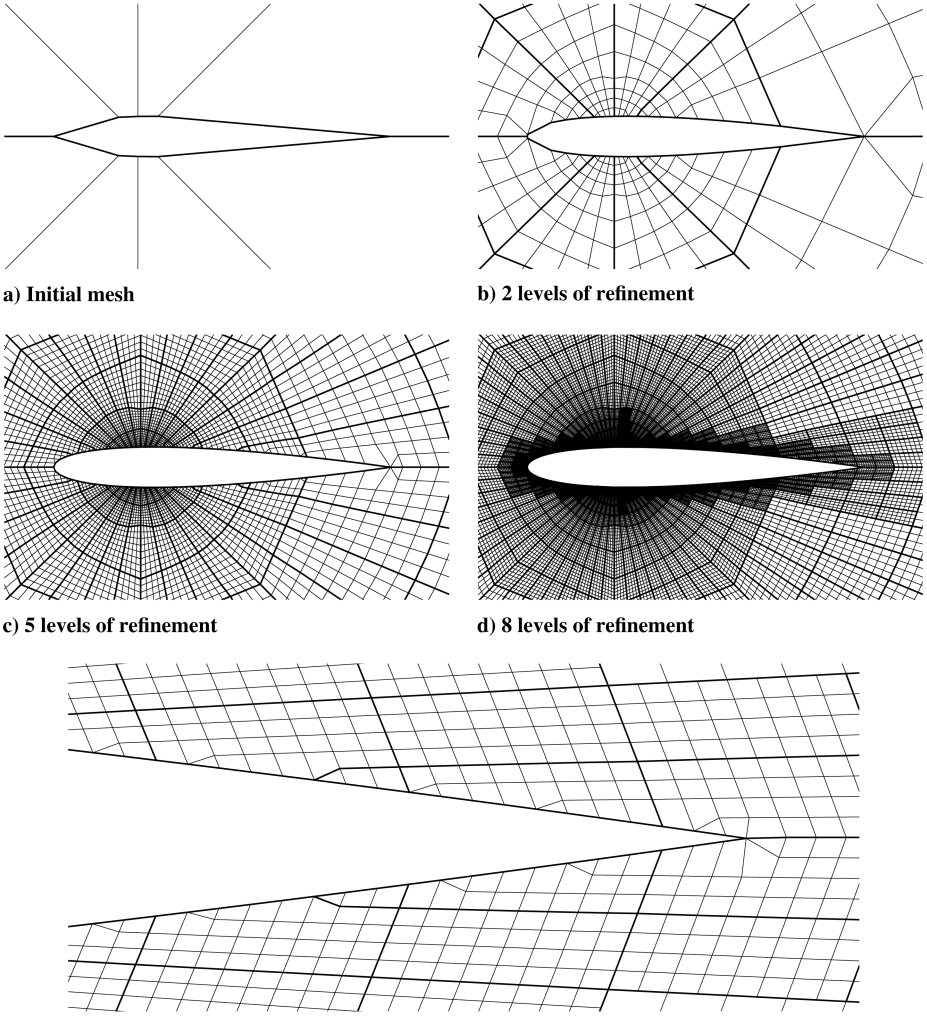

a) Initial mesh

b) 2 levels of refinement

c) 5 levels of refinement

d) 8 levels of refinement

e) 8 levels of refinement, zoom-in

Fig. 17 Multiblock, AMR, computational grid with embedded-boundary treatment for NACA 0012 airfoil.

Once steady state was achieved, the pins were set into motion according to the function $\delta x = \pm\Delta x \sin(2\pi f t)$, where δx is the pin displacement in the x direction from its initial position, Δx is the maximum displacement, t is the time, and $f = 100\ \text{s}^{-1}$ is the frequency of the motion.

Figures 15 and 16 show the predicted distributions of the x-direction velocity component for the branched-channel flow with $Kn = 7 \times 10^{-6}$ and $Kn = 7 \times 10^{-2}$, respectively. In each figure, the results in the top half of the figure show the predicted solutions after 10 ms (one period), whereas the results in the bottom half depict the results after 15 ms (one and a half periods). The geometry at both times is identical; however, at $t = 10$ ms, the two outside rows of pins are approaching the center row, whereas at $t = 15$ ms, the outside rows are moving apart. The differences in the plots indicate that there is some level of hysteresis. It should also be noted that, in the transition-regime case, the hysteresis as well as the general effects of the pins on the flow appear to be significantly reduced. This should be expected since, at higher-Knudsen numbers, the reduced frequency of interparticle collisions leads to a flow that is mostly dependent on the projected area of the cooling pins; something that does not change throughout the simulation.

F. Transonic Flow Past an Oscillating NACA 0012 Airfoil

The final problem considered herein is that of a NACA 0012 airfoil undergoing a prescribed oscillation in a background airflow. The specific problem selected is one studied experimentally by Landon [95] as part of a study of flow conditions for helicopter blades. Here, a NACA 0012 airfoil undergoes an oscillation about its quarter-cord with angle of attack α prescribed by the function

$$\alpha(t) = \alpha_0 + \alpha_m \sin(2\pi f t) \tag{32}$$

where $\alpha_0 = 0.015$ deg, $\alpha_m = 2.51$ deg, and $f = 62.5\ \text{s}^{-1}$. The freestream Reynolds number based on chord length is $Re = 5.5 \times 10^6$, and the freestream Mach number is $Ma = 0.775$. The Knudsen number in this case is $Kn = 6.3 \times 10^{-7}$ and the flow is therefore firmly in the continuum regime. Under these conditions, the flow surrounding the airfoil is expected to be turbulent; however, there is, as yet, no method for the treatment of turbulence in the Gaussian closure. Also, in order to avoid using the number of cells required to predict a boundary layer at such a high Reynolds number, the solid-wall accommodation coefficient was specified to be zero for this case. This is equivalent to assuming fully specular reflection at the boundary and will lead to an inviscid Euler-like near-equilibrium solution using the Gaussian model. To affordably and accurately resolve a boundary layer around the airfoil, an anisotropic mesh-refinement method, as discussed by Zhang and Groth [84], is required. With an anisotropic strategy, resolution could be added normal to the surface without creating a mesh that overresolves the direction along the airfoil surface. Such an approach will eventually be considered as part of the present numerical solution method; however, for now, the accurate resolution of boundary layers for aerodynamic flows such as this is deemed to be too expensive. Given the underresolution of viscous effects for the airfoil, results should not be expected to be entirely physically accurate. Rather, this computation is provided to demonstrate the ease with which the moving-embedded-boundary treatment can be combined with solution-directed adaptive mesh refinement for its eventual application to more practical situations.

The NACA 0012 airfoil boundary was embedded in an O-type grid with the far-field boundary located 16 chord lengths out from the

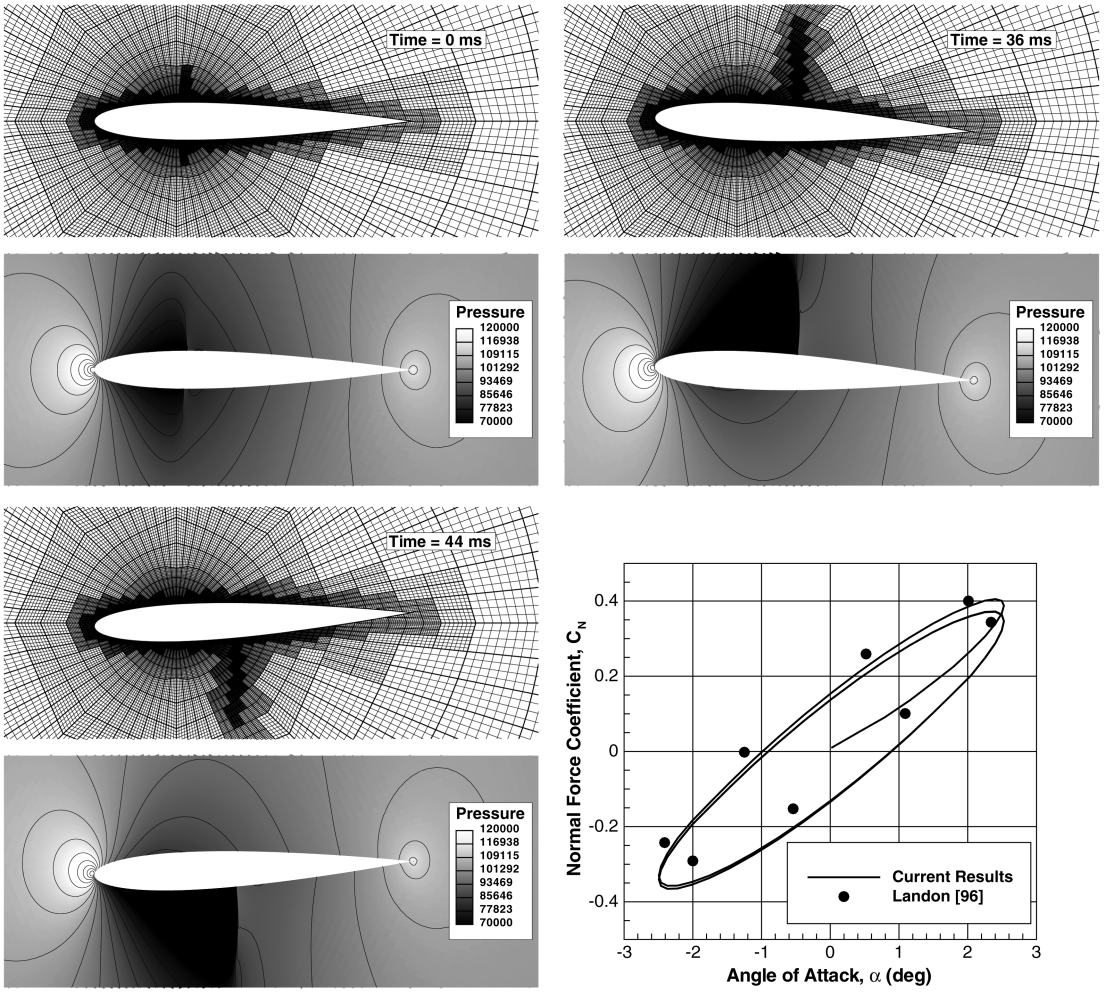

Fig. 18 Numerical prediction of transonic flow past an oscillating NACA 0012 airfoil.

quarter-chord of the airfoil. The far-field boundary conditions were applied in this case by assigning the freestream flow conditions. This initial mesh originally consisted of two 4×8 grid blocks with 64 cells and is depicted in Fig. 17a. This mesh was then refined uniformly twice so as to produce a 32-block grid, as given in Fig. 17b. A regiment of grid sequencing was then employed during which steady-state solutions for flow past the stationary airfoil were sought on sequentially finer meshes leading to a final mesh with eight refinement levels. The successive meshes were obtained either through refinement of every block lying within a bounding box surrounding the airfoil or through solution-directed refinement using the divergence of the velocity field as the refinement criterion (blocks containing high values of the divergence were flagged for refinement, and blocks containing lower values were flagged for possible coarsening). This criterion has been found to identify shocks effectively. The final eight-level AMR mesh resulting from the grid sequencing comprised 3023 blocks and 96,736 cells, 46,797 of which were internal to the airfoil, and therefore inactive. The grid is shown in Fig. 17d. Finally, a zoomed-in view of the trailing-edge region of this final mesh is shown in Fig. 17e. It can be seen that the location of the trailing edge is accurately represented by the modified mesh.

The resulting mesh and steady-state solution from this grid-sequencing procedure was used as the starting point for the time-accurate oscillatory study. For this simulation, adaptive mesh refinement was carried out every 50 time steps. This was found to be of sufficient frequency to allow the grid to track changes in the flow in an effective manner.

The adjusted grid and computed distributions of the thermodynamic pressure for the unsteady problem are shown in Fig. 18. This figure shows the initial steady-state solution as well as the solution $t = 36$ ms and $t = 44$ ms (first and third quarter of the third period of the airfoil pitching motion). It can be observed that, as the airfoil pitches up, the shock on the upper surface strengthens and moves toward the trailing edge, whereas the shock on the lower surface weakens and eventually disappears entirely. As the airfoil pitches down, the opposite is true. The effectiveness with which the adaptive mesh refinement tracks the movement of the shocks can also be plainly seen in Fig. 18. The scheme effectively concentrates blocks, and thus computational cells, along the discontinuity. It is observed that, during the oscillation, there is a hysteresis in the shock position as the airfoil passes the symmetric situation. This hysteresis is reflected in the calculated coefficient of normal force, as seen in the bottom right panel of Fig. 18. In this figure, the computed normal force coefficient moves from a near-symmetric steady-state initial solution to a periodic motion that is in rather good agreement with the experimental results of Landon [95], considering the fact that viscous effects are underresolved and largely ignored in the computation.

V. Conclusions

The potential has been demonstrated for the use of moment closures, combined with an efficient and robust block-based AMR, finite volume scheme and a novel treatment for embedded and moving boundaries, in the numerical solution of continuum- and transition-regime flows. The proposed approach allows for a non-Cartesian body-fitted grid to undergo local adjustments such that it is aligned with arbitrary boundaries. Sharp corners in the interface can be accurately represented, and very small cells, typical of traditional cut-cell approaches, are not introduced. Combined with the purely hyperbolic nature of the moment equations, this allows for accurate treatment of microscale flows and yields solutions that are not strongly affected by grid irregularities arising from the mesh refinement and/or adjustment procedures.

The proposed combined approach has been verified through application to a number of representative two-dimensional flow problems. It has been demonstrated that the hyperbolic nature of moment closures allows for smooth predictions of viscous effects along embedded boundaries for which similar treatments applied to the Navier–Stokes equations yield oscillatory results. Future research will possibly include the extension of the proposed approach to three-dimensional flows and the extension of the Gaussian closure or use of higher-order moment closures to account for the important effects of heat transfer.

Acknowledgments

This research was supported by the Natural Sciences and Engineering Research Council of Canada. Computational resources for performing all of the calculations reported herein were provided by the SciNet High Performance Computing Consortium at the University of Toronto and Compute/Calcul Canada through funding from the Canada Foundation for Innovation and the Province of Ontario, Canada. The authors are very grateful to these funding agencies for this support. The first author would also like to thank the Natural Science and Engineering Research Council of Canada for their generous support of his research through a Canadian Graduate Scholarship.

References

[1] Meyyappan, M. (ed.), *Computational Modeling in Semiconductor Processing*, Artech House, Boston, 1995.

[2] Sun, Q., and Boyd, I. D., "A Direct Simulation Method for Subsonic, Microscale Gas Flow," *Journal of Computational Physics*, Vol. 179, No. 2, 2002, pp. 400–425. doi:10.1006/jcph.2002.7061

[3] Beskok, A., and Karniadakis, G. E., "Simulation of Heat and Momentum Transfer in Complex Microgeometries," *Journal of Thermophysics and Heat Transfer*, Vol. 8, No. 4, 1994, pp. 647–655. doi:10.2514/3.594

[4] Harley, J. C., Huang, Y., Bau, H. H., and Zemel, J. N., "Gas-Flow in Micro-Channels," *Journal of Fluid Mechanics*, Vol. 284, Feb. 1995, pp. 257–274. doi:10.1017/S0022112095000358

[5] Bird, G. A., *Molecular Gas Dynamics and the Direct Simulation of Gas Flows*, Clarendon Press, Oxford, 1994.

[6] Fan, J., and Shen, C., "Statistical Simulation of Low-Speed Rarefied Gas Flow," *Journal of Computational Physics*, Vol. 167, No. 2, 2001, pp. 393–412. doi:10.1006/jcph.2000.6681

[7] Mieussens, L., "Discrete Velocity Model and Implicit Scheme for the BGK Equation of Rarefied Gas Dynamics," *Mathematical Models and Methods in Applied Sciences*, Vol. 10, No. 8, 2000, pp. 1121–1149. doi:10.1142/S0218202500000562

[8] Grad, H., "On the Kinetic Theory of Rarefied Gases," *Communications on Pure and Applied Mathematics*, Vol. 2, No. 4, 1949, pp. 331–407. doi:10.1002/cpa.3160020403

[9] Levermore, C. D., "Moment Closure Hierarchies for Kinetic Theories," *Journal of Statistical Physics*, Vol. 83, Nos. 5–6, 1996, pp. 1021–1065. doi:10.1007/BF02179552

[10] Muller, I., and Ruggeri, T., *Rational Extended Thermodynamics*, Springer-Verlag, New York, 1998.

[11] Struchtrup, H., *Macroscopic Transport Equations for Rarefied Gas Flows*, Springer-Verlag, Berlin, 2005.

[12] Groth, C. P. T., and McDonald, J. G., "Towards Physically-Realizable and Hyperbolic Moment Closures for Kinetic Theory," *Continuum Mechanics and Thermodynamics*, Vol. 21, No. 6, 2009, pp. 467–493. doi:10.1007/s00161-009-0125-1

[13] Godunov, S. K., "Finite-Difference Method for Numerical Computations of Discontinuous Solutions of the Equations of Fluid Dynamics," *Matematicheskii Sbornik*, Vol. 47, 1959, pp. 271–306.

[14] Berger, M. J., "Adaptive Mesh Refinement for Hyperbolic Partial Differential Equations," *Journal of Computational Physics*, Vol. 53, No. 3, 1984, pp. 484–512. doi:10.1016/0021-9991(84)90073-1

[15] Berger, M. J., and Colella, P., "Local Adaptive Mesh Refinement for Shock Hydrodynamics," *Journal of Computational Physics*, Vol. 82, No. 1, 1989, pp. 64–84. doi:10.1016/0021-9991(89)90035-1

[16] De Zeeuw, D., and Powell, K. G., "An Adaptively Refined Cartesian Mesh Solver for the Euler Equations," *Journal of Computational Physics*, Vol. 104, No. 1, 1993, pp. 56–68. doi:10.1006/jcph.1993.1007

[17] Coirier, W. J., and Powell, K. G., "An Accuracy Assessment of Cartesian-Mesh Approaches for the Euler Equations," *Journal of Computational Physics*, Vol. 117, No. 1, 1995, pp. 121–131. doi:10.1006/jcph.1995.1050

[18] Aftosmis, M. J., Berger, M. J., and Melton, J. E., "Robust and Efficient Cartesian Mesh Generation for Component-Based Geometry," *AIAA Journal*, Vol. 36, No. 6, 1998, pp. 952–960. doi:10.2514/2.464

[19] Aftosmis, M. J., Berger, M. J., and Murman, S. M., "Applications of Space-Filling Curves to Cartesian Methods for CFD," AIAA Paper 2004-1232, Jan. 2004.

[20] Sachdev, J. S., Groth, C. P. T., and Gottlieb, J. J., "A Parallel Solution-Adaptive Scheme for Predicting Multi-Phase Core Flows in Solid Propellant Rocket Motors," *International Journal of Computational Fluid Dynamics*, Vol. 19, No. 2, 2005, pp. 159–177. doi:10.1080/10618560410001729135

[21] McDonald, J. G., and Groth, C. P. T., "Numerical Modeling of Micron-Scale Flows Using the Gaussian Moment Closure," AIAA Paper 2005-5035, June 2005.

[22] McDonald, J. G., "Extended Fluid-Dynamic Modelling for Numerical Solution of Micro-Scale," Ph.D. Thesis, Univ. of Toronto, Toronto, 2010.

[23] Sachdev, J. S., and Groth, C. P. T., "A Mesh Adjustment Scheme for Embedded Boundaries," *Computer Physics Communications*, Vol. 2, No. 6, 2007, pp. 1095–1124.

[24] Sachdev, J. S., "Parallel Solution-Adaptive Method for Predicting Solid Propellant Rocket Motor Core Flows," Ph.D. Thesis, Univ. of Toronto, Toronto, April 2007.

[25] Quirk, J. J., and Hanebutte, U. R., "A Parallel Adaptive Mesh Refinement Algorithm," Institute for Computer Applications in Science and Engineering, NASA Langley Research Center Rept. 1993-63, Hampton, VA, Aug. 1993.

[26] Berger, M. J., and Saltzman, J. S., "AMR on the CM-2," *Applied Numerical Mathematics*, Vol. 14, Nos. 1–3, 1994, pp. 239–253. doi:10.1016/0168-9274(94)90028-0

[27] Groth, C. P. T., De Zeeuw, D. L., Powell, K. G., Gombosi, T. I., and Stout, Q. F., "A Parallel Solution-Adaptive Scheme for Ideal Magnetohydrodynamics," AIAA Paper 1999-3273, June 1999.

[28] Groth, C. P. T., De Zeeuw, D. L., Gombosi, T. I., and Powell, K. G., "Global Three-Dimensional MHD Simulation of a Space Weather Event: CME Formation, Interplanetary Propagation, and Interaction with the Magnetosphere," *Journal of Geophysical Research*, Vol. 105, No. A11, 2000, pp. 25053–25078. doi:10.1029/2000JA900093

[29] Coirier, W. J., "An Adaptively-Refined, Cartesian, Cell-Based Scheme for the Euler and Navier–Stokes Equations," Ph.D. Thesis, Univ. of Michigan, Ann Arbor, MI, 1994.

[30] Coirier, W. J., and Powell, K. G., "Solution-Adaptive Cartesian Cell Approach for Viscous and Inviscid Flows," *AIAA Journal*, Vol. 34, No. 5, 1996, pp. 938–945. doi:10.2514/3.13171

[31] Brown, S. L., Roe, P. L., and Groth, C. P. T., "Numerical Solution of a 10-Moment Model for Nonequilibrium Gasdynamics," AIAA Paper 1995-1677, June 1995.

[32] Brown, S. L., "Approximate Riemann Solvers for Moment Models of Dilute Gases," Ph.D. Thesis, Univ. of Michigan, Ann Arbor, MI, 1996.

[33] Chapman, S., and Cowling, T. G., *The Mathematical Theory of Non-Uniform Gases*, Cambridge Univ. Press, Cambridge, England, U.K., 1960.

[34] Burgers, J. M., *Flow Equations for Composite Gases*, Academic Press, New York, 1969.

[35] Gombosi, T. I., *Gaskinetic Theory*, Cambridge Univ. Press, Cambridge, England, U.K., 1994.

[36] Bhatnagar, P. L., Gross, E. P., and Krook, M., "A Model for Collision Processes in Gases. I. Small Amplitude Processes in Charged and Neutral One-Component Systems," *Physical Review*, Vol. 94, No. 3, 1954, pp. 511–525. doi:10.1103/PhysRev.94.511

[37] Torrilhon, M., "Characteristic Waves and Dissipation in the 13-Moment-Case," *Continuum Mechanics and Thermodynamics*, Vol. 12, No. 5, 2000, pp. 289–301. doi:10.1007/s001610050138

[38] Torrilhon, M., "Hyperbolic Moment Equations in Kinetic Gas Theory Based on Multi-Variate Pearson-IV-Distributions," *Communications in Computational Physics*, Vol. 7, No. 4, 2010, pp. 639–673. doi:10.4208/cicp.2009.09.049

[39] Cai, Z., Fan, Y., and Li, R., "Globally Hyperbolic Regularization of Grad's Moment System in One Dimensional Space," *Communications in Mathematical Sciences*, Vol. 11, No. 2, 2013, pp. 547–571. doi:10.4310/CMS.2013.v11.n2.a12

[40] Jaynes, E. T., "Information Theory and Statistical Mechanics," *Physical Review*, Vol. 106, 1957, pp. 620–630. doi:10.1103/PhysRev.106.620

[41] Li, X., Li, M., and Fu, H., "Modeling the Initial Droplet Size Distribution in Sprays Based on the Maximization of Entropy Generation," *Atomization and Sprays*, Vol. 15, No. 3, 2005, pp. 295–322. doi:10.1615/AtomizSpr.v15.i3

[42] Dubroca, B., and Feugeas, J.-L., "Theoretical and Numerical Study on a Moment Closure Hierarchy for the Radiative Transfer Equation," *SIAM Journal on Numerical Analysis*, Vol. 329, No. 10, 1999, pp. 915–920. doi:10.1016/S0764-4442(00)87499-6

[43] Brunner, T. A., and Holloway, J. P., "One-Dimensional Riemann Solvers and the Maximum Entropy Closure," *Journal of Quantitative Spectroscopy and Radiative Transfer*, Vol. 69, No. 5, 2001, pp. 543–566. doi:10.1016/S0022-4073(00)00099-6

[44] Feugeas, J.-L., "A Hierarchy of Nonlocal Models for the Radiative Transfer Equation," *Laser and Particle Beams*, Vol. 22, No. 02, 2004, pp. 121–127. doi:10.1017/S0263034604222066

[45] Berthon, C., Charrier, P., and Dubroca, B., "An HLLC Scheme to Solve the M1 Model of Radiative Transfer in Two Space Dimensions," *SIAM Journal on Scientific Computing*, Vol. 31, No. 3, 2007, pp. 347–389. doi:10.1007/s10915-006-9108-6

[46] Hauck, C. D., "High-Order Entropy-Based Closures for Linear Transport in Slab Geometry," Oak Ridge National Lab. Rept. TM-6023, Oak Ridge, TN, 2010.

[47] Maxwell, J. C., "On the Dynamical Theory of Gases," *Philosophical Transactions of the Royal Society of London*, Vol. 157, 1867, pp. 49–88. doi:10.1098/rstl.1867.0004

[48] Hertweck, F., "Allgemeine 13-Momenten-Näherung zur Fokker-Planck-Gleichung Eines Plasmas," *Zeitschrift für Naturforschung*, Vol. 20a, 1965, pp. 1243–1255.

[49] Oraevskii, V., Chodura, R., and Feneberg, W., "Hydrodynamic Equations for Plasmas in Strong Magnetic Fields—I Collisionless Approximation," *Journal of Plasma Physics*, Vol. 10, No. 9, 1968, pp. 819–828. doi:10.1088/0032-1028/10/9/302

[50] Holway, L. H., Jr., "Approximation Procedures for Kinetic Theory," Ph.D. Thesis, Harvard Univ., Cambridge, MA, 1963.

[51] Holway, L. H., Jr., "Kinetic Theory of Shock Structure Using an Ellipsoidal Distribution Function," *Rarefied Gas Dynamics*, edited by Leeuw, J. H., Vol. 1, Academic Press, New York, 1966, pp. 193–215.

[52] Holway, L. H., Jr., "New Statistical Models for Kinetic Theory: Methods of Construction," *Physics of Fluids*, Vol. 9, No. 9, 1966, pp. 1658–1673. doi:10.1063/1.1761920

[53] Holway, L. H., Jr., "The Effect of Collisional Models upon Shock Wave Structure," *Rarefied Gas Dynamics*, edited by Brundin, C. L., Vol. 1, Academic Press, New York, 1967, pp. 759–784.

[54] McDonald, J. G., and Groth, C. P. T., "Extended Fluid-Dynamic Model for Micron-Scale Flows Based on Gaussian Moment Closure," AIAA Paper 2008-0691, Jan. 2008.

[55] Lam, C. K. S., and Groth, C. P. T., "Numerical Prediction of Three-Dimensional Non-Equilibrium Gaseous Flows Using the Gaussian Moment Closure," AIAA Paper 2011-3401, June 2011.

[56] Suzuki, Y., and van Leer, B., "Application of the 10-Moment Model to MEMS Flows," AIAA Paper 2005-1398, Jan. 2005.

[57] Suzuki, Y., Khieu, L., and van Leer, B., "CFD by First Order PDEs," *Continuum Mechanics and Thermodynamics*, Vol. 21, No. 6, 2009, pp. 445–465. doi:10.1007/s00161-009-0124-2

[58] Barth, T. J., "On Discontinuous Galerkin Approximations of Boltzmann Moment Systems with Levermore Closure," *Computer Methods in Applied Mechanics and Engineering*, Vol. 195, Nos. 25–28, 2006, pp. 3311–3330. doi:10.1016/j.cma.2005.06.016

[59] Junk, M., "Domain of Definition of Levermore's Five-Moment System," *Journal of Statistical Physics*, Vol. 93, Nos. 5–6, 1998, pp. 1143–1167. doi:10.1023/B:JOSS.0000033155.07331.d9

[60] Junk, M., and Unterreiter, A., "Maximum Entropy Moment Systems and Galilean Invariance," *Continuum Mechanics and Thermodynamics*, Vol. 14, No. 6, 2002, pp. 563–576. doi:10.1007/s00161-002-0096-y

[61] Schneider, J., "Entropic Approximation in Kinetic Theory," *Mathematical Modelling and Numerical Analysis*, Vol. 38, No. 3, 2004, pp. 541–561. doi:10.1051/m2an:2004025

[62] Hauck, C. D., Levermore, C. D., and Tits, A. L., "Convex Duality and Entropy-Based Moment Closures: Characterizing Degenerate Densities," *SIAM Journal on Control and Optimization*, Vol. 47, No. 4,

2008, pp. 1977–2015.
doi:10.1137/070691139
[63] Au, J. D., "Lösung Nichtlinearer Problems in der Erweiterten Thermodynamik," Ph.D. Thesis, Technische Univ. Berlin, Berlin, 2001.
[64] McDonald, J. G., and Groth, C. P. T., "Towards Realizable Hyperbolic Moment Closures for Viscous Heat-Conducting Gas Flows Based on a Maximum-Entropy Distribution," *Continuum Mechanics and Thermodynamics*, Vol. 25, No. 5, 2013, pp. 573–603.
doi:10.1007/s00161-012-0252-y
[65] Groth, C. P. T., Gombosi, T. I., Roe, P. L., and Brown, S. L., "Gaussian-Based Moment-Method Closures for the Solution of the Boltzmann Equation," *Proceedings of the Fifth International Conference on Hyperbolic Problems — Theory, Numerics, Applications*, edited by Glimm, J., Graham, M. J., Grove, J. W., and Plohr, B. J.,World Scientific, Hackensack, NJ, 1996, pp. 339–346.
[66] Groth, C. P. T., Roe, P. L., Gombosi, T. I., and Brown, S. L., "On the Nonstationary Wave Structure of a 35-Moment Closure for Rarefied Gas Dynamics," AIAA Paper 1995-2312, June 1995.
[67] Hittinger, J. A., "Foundations for the Generalization of the Godunov Method to Hyperbolic Systems with Stiff Relaxation Source Terms," Ph.D. Thesis, Univ. of Michigan, Ann Arbor, MI, 2000.
[68] Le Tallec, P., "A Hierarchy of Hyperbolic Models Linking Boltzmann to Navier Stokes Equations for Polyatomic Gases," *Zeitschrift für Angewandte Mathematik und Mechanik*, Vol. 80, Nos. 11–12, 2000, pp. 779–789.
doi:10.1002/(ISSN)1521-4001
[69] Struchtrup, H., and Torrilhon, M., "Regularization of Grad's 13 Moment Equations: Derivation and Linear Analysis," *Physics of Fluids*, Vol. 15, No. 9, 2003, pp. 2668–2680.
doi:10.1063/1.1597472
[70] Khieu, L., van Leer, B., and Suzuki, Y., "An Analysis of a Space-Time Discontinous-Galerkin Method for Moment Equations and Its Solid-Boundary Treatment," AIAA Paper 2009-3874, June 2009.
[71] McDonald, J. G., Numerical Modeling of Micron-Scale Flows Using the Gaussian Moment Closure, M.S. Thesis, Univ. of Toronto, Toronto, 2005.
[72] Thomas, P. D., and Lombard, C. K., "Geometric Conservation Laws and Its Application to Flow Computations on Moving Grids," *AIAA Journal*, Vol. 17, No. 10, 1979, pp. 1030–1037.
doi:10.2514/3.61273
[73] Barth, T. J., and Jesperson, D. C., "The Design and Application of Upwind Schemes on Unstructured Meshes," AIAA Paper 1989-0366, Jan. 1998.
[74] Venkatakrishnan, V., "On the Accuracy of Limiters and Convergence to Steady State Solutions," AIAA Paper 1993-0880, Jan. 1993.
[75] Roe, P. L., "Approximate Riemann Solvers, Parameter Vectors, and Difference Schemes," *Journal of Computational Physics*, Vol. 43, No. 2, 1981, pp. 357–372.
doi:10.1016/0021-9991(81)90128-5
[76] Groth, C. P. T., and Northrup, S. A., "Parallel Implicit Adaptive Mesh Refinement Scheme for Body-Fitted Multi-Block Mesh," AIAA Paper 2005-5333, June 2005.
[77] Gao, X., and Groth, C. P. T., "A Parallel Adaptive Mesh Refinement Algorithm for Predicting Turbulent Non-Premixed Combusting Flows," *International Journal of Computational Fluid Dynamics*, Vol. 20, No. 5, 2006, pp. 349–357.
doi:10.1080/10618560600917583
[78] Gao, X., and Groth, C. P. T., "A Parallel Solution-Adaptive Method for Three-Dimensional Turbulent Non-Premixed Combusting Flows," *Journal of Computational Physics*, Vol. 229, No. 5, 2010, pp. 3250–3275.
doi:10.1016/j.jcp.2010.01.001
[79] Gao, X., Northrup, S. A., and Groth, C. P. T., "Parallel Solution-Adaptive Method for Two-Dimensional Non-Premixed Combusting Flows," *Progress in Computational Fluid Dynamics*, Vol. 11, No. 2, 2011, pp. 76–95.
doi:10.1504/PCFD.2011.038834
[80] Northrup, S. A., and Groth, C. P. T., "Solution of Laminar Diffusion Flames Using a Parallel Adaptive Mesh Refinement Algorithm," AIAA Paper 2005-0547, Jan. 2005.
[81] Charest, M. R. J., Groth, C. P. T., and Gülder, O. L., "A Computational Framework for Predicting Laminar Reactive Flows with Soot Formation," *Combustion Theory and Modelling*, Vol. 14, No. 6, 2011, pp. 793–825.
doi:10.1080/13647830.2010.512960
[82] Charest, M. R. J., Joo, H. I., Groth, C. P. T., and Gülder, O. L., "Experimental and Numerical Study of Soot Formation in Laminar Ethylene Diffusion Flames at Elevated Pressures from 10 to 35 atm," *Proceedings of the Combustion Institute*, Vol. 33, No. 1, 2011, pp. 549–557.
doi:10.1016/j.proci.2010.07.054
[83] Sachdev, J. S., Groth, C. P. T., and Gottlieb, J. J., "Parallel AMR Scheme for Turbulent Multi-Phase Rocket Motor Core Flows," AIAA Paper 2005-5334, June 2005.
[84] Zhang, Z. J., and Groth, C. P. T., "Parallel High-Order Anisotropic Block-Based Adaptive Mesh Refinement Finite-Volume Scheme," AIAA Paper 2011-3695, June 2011.
[85] Gropp, W., Lusk, E., and Skjellum, A., *Using MPI*, MIT Press, Cambridge, MA, 1999.
[86] Gropp, W., Lusk, E., and Thakur, R., *Using MPI-2*, MIT Press, Cambridge, MA, 1999.
[87] Bayyuk, S. A., Powell, K. G., and van Leer, B., "A Simulation Technique for 2-D Unsteady Inviscid Flows Around Arbitrarily Moving and Deforming Bodies of Arbitrary Geometry," AIAA Paper 1993-3391, Jan. 1993.
[88] Murman, S. M., Aftosmis, M. J., and Berger, M. J., "Implicit Approaches for Moving Boundaries in a 3-D Cartesian Method," AIAA Paper 2003-1119, Jan. 2003.
[89] Osher, S., and Fedkiw, R., *Level Set Methods and Dynamic Implicit Surfaces*, Vol. 153, Applied Mathematical Sciences, Springer, New York, 2003.
[90] Sethian, J. A., *Level Set Methods and Fast Marching Methods*, 2nd ed., Cambridge Monographs on Applied and Computational Mathematics, Cambridge Univ. Press, Cambridge, England, U.K., 1999.
[91] Schlichting, H., *Boundary-Layer Theory*, 7th ed., McGraw–Hill, Toronto, 1979, pp. 135–144.
[92] Vincenti, W. G., and Kruger, C. H., *Introduction to Physical Gas Dynamics*, R. E. Krieger Publishing, Huntington, NY, 1975, pp. 424–433.
[93] Coudeville, H., Trepaud, P., and Brun, E. A., "Drag Measurements in Slip and Transition Flow," *Rarefied Gas Dynamics*, edited by de Leeuw, J. H., Vol. 1, Academic Press, New York, 1965, pp. 444–466.
[94] Patterson, G. N., *Introduction to the Kinetic Theory of Gas Flows*, Univ. of Toronto Press, Toronto, 1961, pp. 268–284.
[95] Landon, R. H., "Compendium of Unsteady Aerodynamic Measurements," NATO AGARD Advisory Rept. 702, Aug. 1982.

Z. J. Wang
Associate Editor